

Scientific Memoir

Time Reversed Absorbing Conditions in Stratified Media

by

Jeaniffer Vides Higueros

MathMods - Erasmus Mundus MSc Course
University of Nice Sophia-Antipolis

Supervisor: Frédéric Nataf
Laboratoire Jacques-Louis Lions (UMR 7598)

July 21, 2011

Acknowledgements

First and foremost, I offer my sincerest gratitude to my supervisor, Frédéric Nataf, for giving me the opportunity to experience the thrill of doing research at Laboratoire Jacques-Louis Lions. With his enthusiasm, his inspiration, and his great efforts to explain things clearly, he made this academic experience invaluable to me. I would like to thank Marie Kray for her dedicated support and encouragement during my time at the laboratory and for tutoring me these past five months. I would also like to thank my coordinator and guide, Professor Pierre-Emmanuel Jabin, for his constant advice and assistance. My heartfelt thanks to my best friend Maria Laura, who always makes sure I feel her confidence and encouragement.

This thesis is dedicated to my parents and sister. I acknowledge the love, moral and emotional support they have given me throughout all the stages in my life, and, despite the geographical distance, they have always been nearby. None of this could have happened without them.

Contents

1	Introduction	6
1.1	Need for Absorbing Boundary Conditions	7
1.1.1	Mathematical Details	9
1.2	Time Reversed Absorbing Conditions	10
2	Background Theory	11
2.1	Electromagnetic Wave Equation	11
2.1.1	Maxwell's Equations and Constituent Relations	11
2.1.2	Electrical and Magnetic Properties of the Medium	11
2.1.3	Electric Wave Equation with Constant Coefficients	14
2.1.4	Scalar Component of the Electric Field	15
2.1.5	Electric Wave Equation in a Stratified Medium	16
2.1.6	Plane Wave Reflection/Transmission at a Dielectric Interface	17
2.2	Anti-Personnel Mines	18
2.2.1	Fragmentation Mines	18
2.2.2	Blast Mines	19
3	Modeling	20
3.1	Principle of the TRAC Method	21
3.2	Energy Estimate	23
3.3	Recreating the Past	25
3.4	Numerical Approximation	26
3.4.1	Forward Problem	26
3.4.2	Time Reversed BVP	29
3.5	Criteria	33
3.5.1	Absorbing Boundary Condition Criterion	33
3.5.2	Cross-Correlation Criterion	34
4	Numerical Results	35
4.1	Two Layers	35
4.1.1	Iron Objects	37
4.1.2	Plastic Objects	40
4.2	Three Layers	44
4.2.1	Shifting the Enclosing Ellipse	45
5	Conclusions	49

List of Tables

1	Typical values of static conductivity and relative permittivity (real component) derived from experiment for common subsurface materials at an antenna frequency of 100MHz	13
2	Values for the dielectric permittivity and magnetic permeability of five materials	36
3	Impedances and propagation speeds in five selected materials	36
4	Results of two relative criteria in the case of distant iron objects	39
5	Results of two relative criteria in the case of close iron objects	40
6	Results of two relative criteria in the case of distant plastic objects	41
7	Results of two relative criteria in the case of close plastic objects	41
8	Non relative cross-correlation criterion for distant iron vs. plastic objects in a two-layered medium.	43
9	Non relative cross-correlation criterion for close iron vs. plastic objects in a two-layered medium.	43
10	Non relative cross-correlation criterion for an iron mine enclosed by an ellipse, in a three-layered medium	46
11	Results of the relative cross-correlation criterion for an iron mine enclosed by an ellipse, in a three-layered medium	47

List of Figures

1	Experimental setup proposed by M. Fink	6
2	Vertical component of the Sumatra-Andaman time reversed field at different times	7
3	Forward problem for the Sumatra-Andaman earthquake	8
4	Classical time reversal method applied to the Sumatra-Andaman model	8
5	Expected results from the time reversed Sumatra-Andaman problem	9
6	Geometry of a reflection/transmission problem	17
7	Domain geometry for the generic model	20
8	Two configurations of the source-receiver array (SRA)	25
9	Model geometry	26
10	Setup for a two-layered medium	35
11	Imaging function in a two-layered medium for distant iron objects	38
12	Imaging function in a two-layered medium for close iron objects	38
13	Imaging function in a two-layered medium for close iron objects	42
14	Imaging function in a two-layered medium for distant plastic objects	42
15	Setup for a three-layered medium	44
16	Setup for the mine and ellipse in a new coordinate system	46
17	Relative cross-correlation criterion as a function of the shift	47
18	Imaging function in a three-layered medium for an iron mine buried in sand	48

1 Introduction

Time reversibility is a subject of very active research. Although classical and quantum mechanics equations are reversible at a microscopic scale, it is known that macroscopic phenomena are irreversible [12]. One of the reasons for this apparent irreversibility is the particularly large number of particles that comprise macroscopic systems. In classical mechanics, the evolution of a system is extremely sensitive to its initial conditions and the slightest error in the model would make time reversing not possible. It would be then necessary to have an infinite amount of information to make an accurate model and this is unrealizable with any real experimental device.

In wave physics, the amount of information necessary to describe a wave field explicitly is limited and depends on the shortest wavelength of the field, making it feasible and easier to perform time reversal experiments with waves rather than with particles. However, even though reversibility of physical phenomena is a simple idea, making it an experimental fact is far less evident.

The main idea of time reversal is to take advantage of the reversibility of wave propagation phenomena such as it occurs in acoustics or electromagnetism, in a non-dissipative but unknown medium in order to back-propagate signals to the sources that emitted them. In 1992, Mathias Fink proposed an experiment consisting of the transmission of a signal through a complex medium, a barrier composed of randomly distributed metal rods. The scattered field is then recorded using a TRM (time reversal mirror) array, an array of N wide-band piezoelectric transducers that perform a fine spatial sampling of the field. The N recorded signals are placed in memory, reversed in time, and sent back through the barrier by the TRM array. The aim of the experiment is to refocus the signal precisely, as shown in figure 1, even without not knowing the location of the barriers.

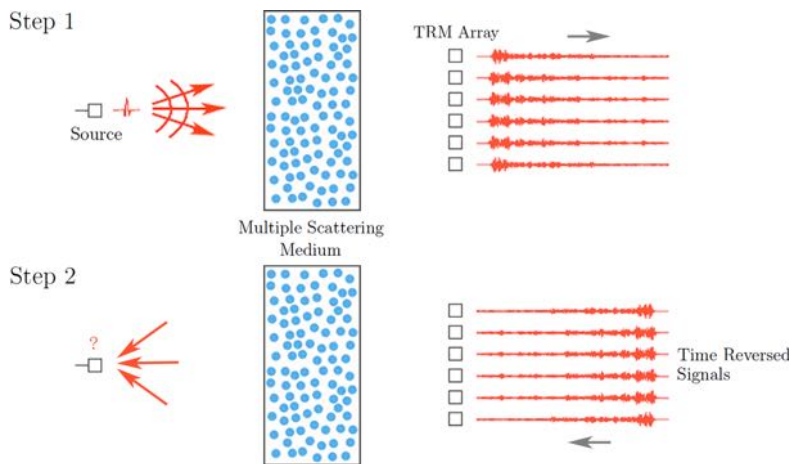


Figure 1: Experimental setup. First step (top): the source sends a pulse through the barrier and the scattered wave is recorded by the TRM array. Second step (bottom): the signals have been time reversed and are retransmitted by the TRM array through the barrier with the aim of being refocused precisely.

There have been numerous applications of this physical principle in medical imaging or therapy, marine acoustics, and waves in complex media, among others, see [13] and references therein. The first mathematical analysis for a homogeneous medium can be found in [4] and for a random medium in [8] and [11]. In this paper, we focus on stratified media.

1.1 Need for Absorbing Boundary Conditions

One of the applications for the time reversal method proposed by Jean-Paul Montagner et al. is locating the epicenter of an earthquake. They performed time reversal imaging of seismic sources and applied it to the great Sumatra-Andaman earthquake, see [15].

On December 26, 2004, an undersea megathrust earthquake occurred at 00:58:53 UTC, with its epicentre off the west coast of Sumatra, Indonesia. The earthquake itself is known by the scientific community as the Sumatra-Andaman earthquake. It had one of the longest duration of faulting ever observed and the event lasted about 6-7 minutes. After the deconvolution of the instrument response and a pass-band frequency filtering, 165 stations were chosen for the good quality of their vertical records.

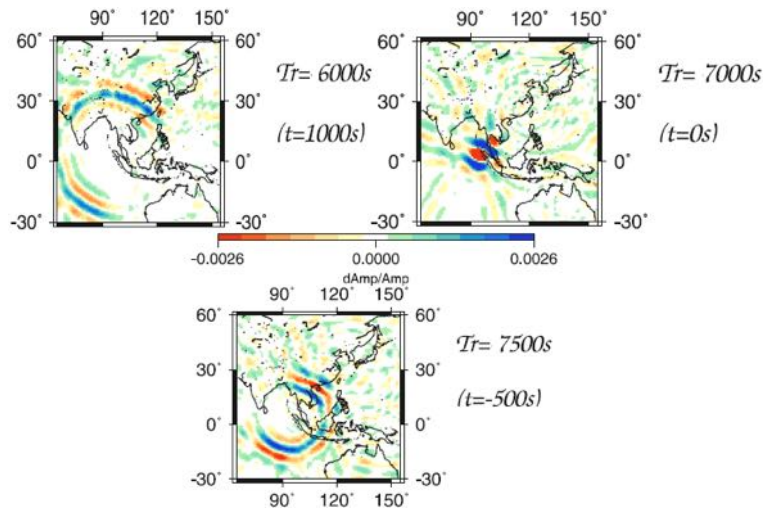


Figure 2: Vertical component of the time reversed field at different times for the Sumatra-Andaman event. The absolute real time is given by t ; Tr is the reversed time and $Tr = 7000s$ is the source initial time ($t = 0s$).

M. Fink et al. applied a time reversal method to the obtained data. Hence, the initial time of the earthquake corresponds to $t_0 = 0s$, i.e., to a reversed time $Tr = 7000s$. The idea is to create an exact time reversed replica of the earthquake. Figure 2 shows three snapshots of the time reversed wavefield at different times $Tr = 6000s, 7000s$ and $7500s$. It is evident that the waves do not stop after focusing but continue to propagate displaying an almost circular wavefront, i.e., the waves should have stopped at time $7000s$ ($t = 0s$). Hence, the exact time reversed replica of experiment is not created.

This numerical experiment is useful to understand one problem encountered when using time reversal methods, i.e., the incapability of refocusing the signal precisely. In figure 2, we can see a diffraction spot around the source at time 7000s and, most importantly, the continued wave propagation after this time. To find the reason, we take a closer look at the problem by analyzing it by parts: forward problem data, classical time reversal method, and expected results.

Forward Problem Data

We set the initial time of the earthquake $t_0 = 0$ s to be the time when the earthquake originated. It is then clear that for times $t < 0$ s we have no signal, as shown in figure 3(a). At the initial time, the earthquake occurs and there is a sudden release of energy in the Earth's crust, creating seismic waves. These circular and diverging waves propagate away from the epicenter until they exit a window chosen for the analysis.

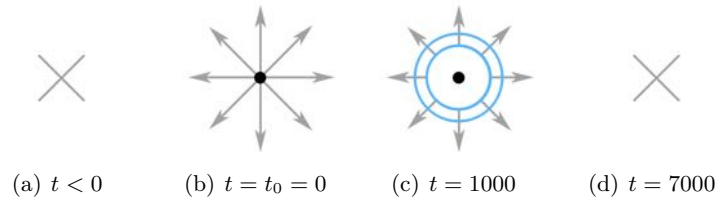


Figure 3: Forward problem. (a) No seismic waves before the earthquake. (b) Earthquake occurs and diverging seismic waves are created. (c) Seismic waves propagate and exit the chosen window. (d) No seismic waves present in the window.

Classical Time Reversal Method

The principle of the time reversal method applied by M. Fink is to send back the forward field and to refocus the signal precisely, even without not knowing the location of the source. However, the converging waves do not stop after focusing but begin to diverge, as shown in figure 4(c). This creates interference between the diverging and converging waves. Additionally, after time $Tr = 7000$ s, we observe diverging waves that should not exist.

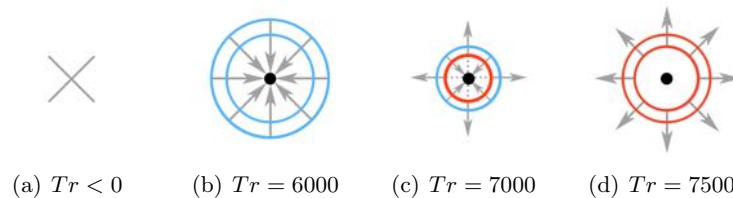


Figure 4: Classical time reversal method applied to the Sumatra-Andaman model. (a) No seismic waves present. (b) Seismic waves converge towards the source. (c) Interference between diverging and converging waves is evident. (d) Only diverging waves remain.

Expected Results

As we have mentioned several times before, the aim of the method is to send back the forward field and to focus the signal precisely at the source, as shown in figure 5.

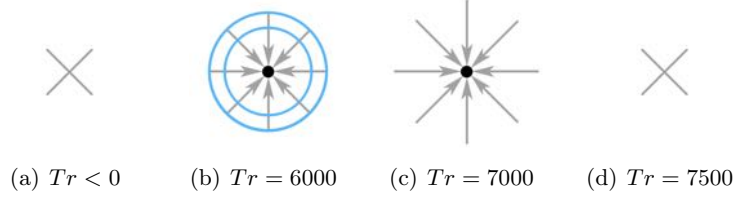


Figure 5: Expected results. (a) No seismic waves present in the window. (b) Waves converge towards the source. (c) No interference occurs and the waves converge exactly at the epicenter. (d) No seismic waves present.

We can infer that the problem with the classical time reversal method is due to the fact that the source is not replaced by its time reversed version, i.e., it is necessary to have a sink to absorb all the converging front.

1.1.1 Mathematical Details

Using a simplified notation, we can write the forward problem as

$$Elasto(u(t, x)) = f(t)\mathbf{1}_{epicenter}, \quad x \in \mathbf{R}^2, \quad t > 0,$$

where $u(t, x)$ is the displacement field, $f(t)$ is a function with compact support corresponding to the earthquake, and $Elasto$ represents the function for the elastic seismic wave. We consider homogeneous Cauchy data for this model.

Using the same notation as M. Fink et al., where Tr is the reversed time, and denoting the final time as T_f , the time reversal problem obtained with the classical method has the form

$$\begin{cases} Elasto(u^R(Tr, x)) = 0, & x \in \mathbf{R}^2, \quad Tr > 0, \\ u^R(0, x) = u(T_f, x). \end{cases}$$

However, in order to acquire the expected results, the time reversal problem should be

$$\begin{cases} Elasto(u^R(Tr, x)) = f(T_f - Tr)\mathbf{1}_{epicenter}, & x \in \mathbf{R}^2, \quad Tr > 0, \\ u^R(0, x) = u(T_f, x). \end{cases} \quad (1.1)$$

The function f is unknown and the location of the epicenter is only approximately known, making problem (1.1) unsolvable. It is then necessary to find f by solving an inverse problem

or use absorbing boundary conditions, i.e., non-reflecting conditions. In this paper, we take the absorbing boundary conditions approach.

1.2 Time Reversed Absorbing Conditions

An absorbing boundary condition (ABC) is frequently used to limit the computational domain in simulations over unbounded domains. The basic requirements for these types of boundary conditions are stability, accuracy and computational efficiency. Accuracy refers to the true solution satisfying the ABC. It is clearly necessary to have well posedness of the initial boundary value problem and stability of the corresponding computational algorithm.

Depending on the desired application, absorbing boundary conditions go under many names, e.g., radiation, far field or open. Hence, it is possible to model an unbounded domain using a far field boundary condition on an artificial outer surface.

We are interested in the Time Reversed Absorbing Conditions (TRAC) introduced in [1], [2], and [3]. These types of boundary conditions let us "recreate the past" without knowing the location and properties of an inclusion present in the medium. Since inclusions tend to diffract the wave travelling through the medium, the TRAC method makes the recreation possible by removing a small region surrounding the scattering inclusion. This technique has two applications in inverse problems: the reduction of the size of the computational domain and the determination of an unknown inclusion's location from boundary measurements. The TRAC method is designed in both the time-dependent and harmonic domains.

In this paper, we extend the TRAC method by considering a medium composed of a stack of two or three layers made of homogeneous media. We use the method to differentiate between two close inclusions and one single inclusion. In contrast to many inverse problem methods, the TRAC method does not rely on any *a priori* knowledge of the inclusion's physical properties, i.e., hard, soft and penetrable inclusions are all treated in the same way.

The outline of the paper is as follows. In the next section, we give background theory that will be useful to understand the electric wave equation and its related terms. We also present the basic theory of antipersonnel-mines. In Section 3, we recall the principle of the TRAC method for the time dependent wave equation. We also define the model that will recreate the past from boundary measurements in stratified media and we give its discretization in time and space. In Section 4, we describe two experiments and analyze their corresponding numerical results.

2 Background Theory

2.1 Electromagnetic Wave Equation

In this paper, we will make use of the electromagnetic wave. Its propagation through a medium or vacuum is described by the electromagnetic wave equation, a second-order partial differential equation derived from Maxwell's equations. For the moment, we consider the three-dimensional space \mathbf{R}^3 to be the propagation medium.

2.1.1 Maxwell's Equations and Constituent Relations

In modern physics, Maxwell's derivation of the electromagnetic wave equation has been replaced by a more straightforward method involving the combination of the corrected version of Ampère's circuital law with Faraday's law of induction. The unknowns are the electric field $E(t, x)$, the magnetic field $H(t, x)$, the electrical induction $D(t, x)$, and the magnetic induction $B(t, x)$, at point $x \in \mathbf{R}^3$ and time $t \geq 0$. In the absence of charges and currents, these variables satisfy Maxwell's equations given by

$$\left\{ \begin{array}{l} \nabla \times E = -\frac{\partial B}{\partial t}, \\ \nabla \times H = \frac{\partial D}{\partial t}, \\ \nabla \cdot D = 0, \\ \nabla \cdot B = 0. \end{array} \right. \quad (2.2)$$

The equations presented in (2.2) are written in their classical, time domain, differential form and the physical quantities shown are related by two constitutive equations

$$\left\{ \begin{array}{l} B(t, x) = \mu(x)H(t, x), \\ D(t, x) = \varepsilon(x)E(t, x), \end{array} \right. \quad (2.3)$$

where $\mu(x)$ is the magnetic permeability and $\varepsilon(x)$ is the dielectric permittivity of the medium.

2.1.2 Electrical and Magnetic Properties of the Medium

The constitutive relations studied in the previous section introduced the relevant material property parameters of permittivity and magnetic permeability. The common property known as conductivity is not of interest for this paper, since we are not considering conduction currents. Therefore, we will only give the definition and some basic information about this parameter.

We are interested in electric waves propagating through vacuum or subsurface materials. These materials are usually described as dielectrics, with the parameters permittivity and conductivity

loosely named their "dielectric properties". However, since subsurface materials possess some form of free charge, such as conduction electrons and ions, they can be best described as lossy dielectrics and not true dielectrics.

Permittivity and Conductivity

From the classical point of view, permittivity relates to the storage ability of capacitors since it describes the ability of a material to store and release electromagnetic energy in the form of electric charge. Alternatively, it can be described as the ability to restrict the flow of free charges or the degree of polarization exhibited when forming an electric field in a material. Thus, permittivity relates to a material's ability to transmit an electric field and it is usually used in terms of a nondimensional, relative permittivity term ε_r , defined by

$$\varepsilon_r = \frac{\varepsilon}{\varepsilon_0}, \quad (2.4)$$

being ε the permittivity of the material and ε_0 the one of free space or vacuum. The latter has a value of 8.8542×10^{-12} F/m (farads per meter) and differs negligibly from the permittivity of air. In some literature, the relative permittivity is referred to as the "dielectric constant" and is represented by the symbol κ .

In the presence of free and bound water, the permittivity of subsurface materials can vary dramatically. Additionally, as opposed to the response of vacuum, the response of materials to external fields generally depends on the frequency of the field. This is the reason why permittivity is often treated as a frequency angular-dependent complex function $\hat{\varepsilon}(\omega)$, with real and imaginary components,

$$\hat{\varepsilon}(\omega) = \varepsilon'(\omega) + i\varepsilon''(\omega),$$

where the real part $\varepsilon'(\omega)$ is related to the stored energy and the imaginary part $\varepsilon''(\omega)$ to the dissipation or loss of energy within the medium. These terms depend on the angular frequency ω . In the case of lossy media, i.e., when the conduction current is not negligible, the complex permittivity is defined as

$$\hat{\varepsilon}(\omega) = \varepsilon'(\omega) + i\frac{\sigma}{\omega},$$

with σ representing the conductivity of the medium and i the imaginary unit ($i^2 = -1$). In simple terms, conductivity describes a material's ability to conduct or pass free electric charges under the influence of an applied field. At low frequencies, the charge response is effectively instantaneous, allowing the conduction current to be in phase with the electric field. Hence, conductivity is usually represented by a real, static value σ_s measured in S/m.

Table 1 lists the relative permittivity and conductivity of some common subsurface materials at a frequency of 100 MHz and their typical range under natural conditions. The values shown are derived from experiment and illustrate the influence of free and bound water, i.e., the values increase as the material gets wetter or decrease as it gets drier.

However, although permittivity is a complex quantity, the permittivity value of a material is often simplified to its constant, low-frequency or static real component with the loss term ignored.

Material	Static Conductivity $\sigma_s(mS/m)$	Relative Permittivity ϵ_{ave}
Air	0	1
Clay - dry	1-100	2-20
Clay - wet	100-1000	15-40
Concrete - dry	1-10	4-10
Concrete - wet	10-100	10-20
Freshwater	0.1-10	78(25°C)-88
Freshwater ice	1-0.000001	3
Seawater	4000	81-88
Seawater ice	10-100	4-8
Permafrost	0.1-10	2-8
Granite - dry	0.001-0.00001	5-8
Granite - fractured and wet	1-10	5-15
Limestone - dry	0.001-0.0000001	4-8
Limestone - wet	10-100	6-15
Sandstone - dry	0.001-0.0000001	4-7
Sandstone - wet	0.01-0.001	5-15
Shale - saturated	10-100	6-9
Sand - dry	0.0001-1	3-6
Sand - wet	0.1-10	10-30
Sand - coastal, dry	0.01-1	5-10
Soil - sandy, dry	0.1-100	4-6
Soil - sandy, wet	10-100	15-30
Soil - loamy, dry	0.1-1	4-6
Soil - loamy, wet	10-100	10-20
Soil - clayey, dry	0.1-100	4-6
Soil - clayey, wet	100-1000	10-15
Soil - average	5	16

Table 1: Typical values of static conductivity and relative permittivity (real component) derived from experiment for common subsurface materials at an antenna frequency of 100MHz (table obtained from Cassidy, Nigel J).

Magnetic Permeability

In electromagnetism, the term permeability refers to the measure of the material's ability to support the formation of a magnetic field within itself. Put simply, it is the degree of magnetization that a material obtains in response to an applied magnetic field and it is usually used in terms of a nondimensional, relative permeability term denoted by the symbol μ_r . This

term is given by the ratio of the medium's permeability μ to the one of free-space μ_0 , which has a value of $4\pi \times 10^{-7} \approx 1.2566 \times 10^{-6}$ H/m. Thus,

$$\mu_r = \frac{\mu}{\mu_0}. \quad (2.5)$$

It is known for ferromagnetic minerals to have significant magnetic permeabilities, which vary greatly with the strength of the applied magnetic field. However, in most common subsurface geological materials, the amount of ferromagnetic material is considered unimportant since it is typically below 2%, see [9]. In these circumstances, when the magnetic effect of materials has little effect on the wave, their magnetic permeability μ is often simplified to the free-space value.

2.1.3 Electric Wave Equation with Constant Coefficients

We consider the case where magnetic permeability and dielectric permittivity functions are constant, i.e., $\mu(x) = \mu$ and $\varepsilon(x) = \varepsilon$, $\forall x \in \mathbf{R}^3$, being μ and ε the two positive scalars which characterize the electromagnetic behavior of the homogeneous medium where the wave propagates. We recall that we are working with time $t \geq 0$.

By computing the time derivate of (2.3), we get

$$\begin{cases} \frac{\partial B(t, x)}{\partial t} = \mu \frac{\partial H(t, x)}{\partial t}, \\ \frac{\partial D(t, x)}{\partial t} = \varepsilon \frac{\partial E(t, x)}{\partial t}. \end{cases} \quad (2.6)$$

Using (2.6) and Maxwell's equations given by (2.2), we can verify that

$$\varepsilon \frac{\partial E}{\partial t} = \nabla \times H, \quad (2.7)$$

$$\mu \frac{\partial H}{\partial t} = -\nabla \times E. \quad (2.8)$$

We focus our attention on the electric field $E(t, x)$. By computing the time derivative of (2.7) and using equation (2.8), we finally obtain the homogeneous form of the electromagnetic wave equation in terms of the electric field

$$\varepsilon \frac{\partial^2 E}{\partial t^2} - \nabla \cdot \left(\frac{1}{\mu} \nabla E \right) = 0, \quad (2.9)$$

which can be written in terms of the constant propagation speed of light $c = \sqrt{\frac{1}{\mu\varepsilon}}$ in the medium and the vector Laplace operator ∇^2 . Hence, the wave equation takes the form

$$\frac{\partial^2 E}{\partial t^2} - c^2 \cdot \nabla^2 E = 0. \quad (2.10)$$

We notice that equation (2.10) is time reversible, i.e., the function $E(-t, x)$ is also a solution to this equation due to the second order time derivative where

$$\frac{\partial^2 E(-t, x)}{\partial t^2} = \frac{\partial^2 E(t, x)}{\partial t^2}.$$

This property also holds true for acoustic and elastic (e.g., seismic) wave equations since they are all hyperbolic equations without dissipation. However, it is clear that it does not hold for parabolic equations, e.g., the heat equation, due to the first order time derivative. Thus,

$$\frac{\partial E(-t, x)}{\partial t} = -\frac{\partial E(t, x)}{\partial t} \neq \frac{\partial E(t, x)}{\partial t}.$$

2.1.4 Scalar Component of the Electric Field

The electric field solved by equation (2.9) is a vector field with SI units of newtons per coulomb (N/C) or, equivalently, volts per meter (V/m). In this paper, we will only work with one of the components of this field and it will be represented by u . Hence, in a two-dimensional medium, u is the scalar solution of the wave equation

$$\varepsilon(x) \frac{\partial^2 u(t, x)}{\partial t^2} - \nabla \cdot \left(\frac{1}{\mu(x)} \nabla u(t, x) \right) = 0, \quad x \in \mathbf{R}^2, \quad t > 0, \quad (2.11)$$

We recall that in a strictly homogeneous medium, the permittivity and magnetic permeability are constants. Equation (2.11) has a form similar to the acoustic wave equation given by

$$\frac{1}{K(x)} \frac{\partial^2 p(t, x)}{\partial t^2} - \nabla \cdot \left(\frac{1}{\rho(x)} \nabla p(t, x) \right) = 0, \quad x \in \mathbf{R}^2, \quad t > 0, \quad (2.12)$$

where $p(t, x)$ is the acoustic pressure field, $\rho(x)$ the density function and $K(x)$ is known as the bulk modulus function. The acoustic wave equation governs the propagation of acoustic waves through a medium, i.e., it describes the evolution of the acoustic pressure as a function of time and space. It is then clear that equation (2.11) has the form of an acoustic wave equation with electromagnetic coefficients.

Cauchy Problem

The initial value problem for (2.11) is given by

$$\begin{cases} \varepsilon(x) \frac{\partial^2 u}{\partial t^2} - \nabla \cdot \left(\frac{1}{\mu(x)} \nabla u \right) = 0, & x \in \mathbf{R}^2, \quad t > 0, \\ u(0, x) = u_0(x), & x \in \mathbf{R}^2, \\ \frac{\partial u(0, x)}{\partial t} = u_1(x), & x \in \mathbf{R}^2. \end{cases} \quad (2.13)$$

2.1.5 Electric Wave Equation in a Stratified Medium

We now study the case where the medium varies in a piecewise-constant manner, i.e., we consider a stack of layers made of homogeneous media. This section begins with the case of two layers which can be easily extended to the three-layer case.

Two Layers

The initial value problem (or, Cauchy problem) takes the form

$$\begin{cases} \varepsilon(x) \frac{\partial^2 u}{\partial t^2} - \nabla \cdot \left(\frac{1}{\mu(x)} \nabla u \right) = 0, & x = (x_1, x_2) \in \mathbf{R}^2, \quad t > 0, \\ u(0, x) = u_0(x), & x \in \mathbf{R}^2, \\ \frac{\partial u(0, x)}{\partial t} = u_1(x), & x \in \mathbf{R}^2, \end{cases} \quad (2.14)$$

where the propagation medium consists of two semi-infinite homogeneous media separated by an interface at $x_2 = \text{constant} = h$, i.e., the magnetic permeability and dielectric permittivity functions are defined by

$$\varepsilon(x) = \begin{cases} \varepsilon_1 & \text{if } x_2 > h, \\ \varepsilon_2 & \text{if } x_2 < h, \end{cases} \quad \mu(x) = \begin{cases} \mu_1 & \text{if } x_2 > h, \\ \mu_2 & \text{if } x_2 < h. \end{cases} \quad (2.15)$$

Additionally, for each homogeneous layer, we can obtain the corresponding propagation speeds $c_1 = \sqrt{1/(\mu_1 \varepsilon_1)}$ and $c_2 = \sqrt{1/(\mu_2 \varepsilon_2)}$. The propagation speed function reads

$$c(x) = \begin{cases} c_1 & \text{if } x_2 > h, \\ c_2 & \text{if } x_2 < h. \end{cases}$$

Three Layers

We consider now the case where we have a stack of three layers of homogeneous media separated by two interfaces at $x_2 = \alpha$ and $x_2 = \beta$, both constants satisfying $\alpha < \beta$. We recall that this problem is an extension of the two-layer case. Hence, the Cauchy problem takes the same form as (2.14) with magnetic permeability and dielectric permittivity functions given by

$$\varepsilon(x) = \begin{cases} \varepsilon_1 & \text{if } x_2 > \alpha, \\ \varepsilon_2 & \text{if } x_2 \in (\alpha, \beta), \\ \varepsilon_3 & \text{if } x_2 < \beta, \end{cases} \quad \mu(x) = \begin{cases} \mu_1 & \text{if } x_2 > \alpha, \\ \mu_2 & \text{if } x_2 \in (\alpha, \beta), \\ \mu_3 & \text{if } x_2 < \beta. \end{cases} \quad (2.16)$$

The corresponding propagation speed function has the form

$$c(x) = \begin{cases} c_1 = \sqrt{\frac{1}{\mu_1 \varepsilon_1}} & \text{if } x_2 > \alpha, \\ c_2 = \sqrt{\frac{1}{\mu_2 \varepsilon_2}} & \text{if } x_2 \in (\alpha, \beta), \\ c_3 = \sqrt{\frac{1}{\mu_3 \varepsilon_3}} & \text{if } x_2 < \beta. \end{cases}$$

2.1.6 Plane Wave Reflection/Transmission at a Dielectric Interface

Since we are dealing with stratified media, let us introduce the concept of plane wave reflection and transmission at a dielectric interface. In the physics of wave propagation, a plane wave is a constant-frequency wave whose wavefronts are infinite parallel planes of constant amplitude normal to the phase velocity vector. These waves are particular solutions of the wave equation.

In general, a wave experiences partial transmittance and partial reflectance when the medium through which it is propagating changes. We consider the case where a plane wave travels through a homogeneous medium and encounters an interface with a different medium. At the interface, a portion of the wave is reflected while the remainder of the wave is transmitted, as shown in figure 6.

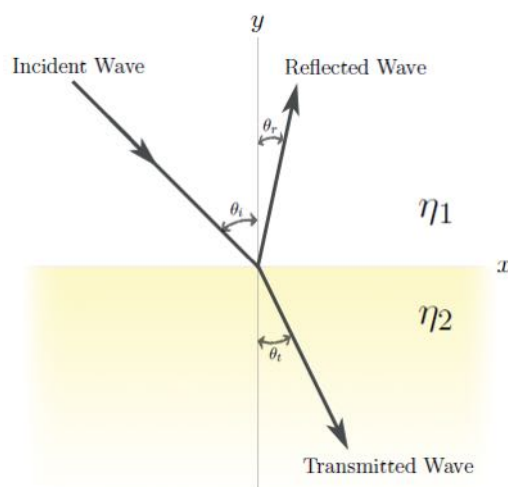


Figure 6: Geometry of a reflection/transmission problem.

By enforcing the electromagnetic field boundary conditions at the media interface, the reflected and transmitted waves can be determined. We then solve for the reflection coefficient Γ and transmission coefficient τ , given by

$$\Gamma = \frac{\eta_2 - \eta_1}{\eta_2 + \eta_1}, \quad \tau = \frac{2\eta_2}{\eta_2 + \eta_1}, \quad (2.17)$$

where η_1 and η_2 are the wave impedances of the electromagnetic wave in the first and second medium, respectively. The wave impedance corresponds to the ratio of the transverse components of the electric and magnetic fields traveling through a medium and it has the form

$$\eta = \sqrt{\frac{i\omega\mu}{\sigma + i\omega\varepsilon}}. \quad (2.18)$$

In the case of a dielectric medium, equation (2.18) reduces to

$$\eta = \sqrt{\frac{\mu}{\varepsilon}}. \quad (2.19)$$

2.2 Anti-Personnel Mines

Anti-personnel mines are a form of mines, which, as the name implies, are designed for use against enemy personnel and are activated by pressure, tripwire or remote detonation. They are designed to kill or injure as many victims as possible. Hence, humans are the target as opposed to anti-tank mines, which are designed for use against vehicles.

There are several-hundred different kinds of anti-personnel mines in use by many countries which can be classified in numerous ways. However, they all fit into two basic categories: fragmentation and blast.

2.2.1 Fragmentation Mines

Fragmentation mines are designed to project fragments in all directions or in one direction (directional fragmentation mines), causing shrapnel wounds to nearby personnel. These mines can cause injury up to 200 meters away and kill at closer distances with fragments which are either glass or metal. Fragmentation mines can be bounding or ground-based. The latter are not of interest for this paper.

Bounding mines are designed to be used in open areas and are usually buried with only a small part of the igniter protruding from the ground, making these mines pressure or tripwire activated. These mines are also referred to as "Bouncing Betty". When activated, a small propelling charge launches the body of the mine about one meter into the air. The mine then ignites a main charge, spraying fragmentation and causing injury around the person's waist, head and chest.

This type of mine is designed to be buried and it usually contains a large amount of steel, making it relatively easy to detect with metal detectors. However, it is common for other minimum metal mines to be planted in the same minefield, which complicates the demining process.

2.2.2 Blast Mines

Anti-personnel blast mines, the most common type of mine, are typically pressure activated, i.e., they are triggered when the victim steps on the pressure plate. The minimum weight needed to activate them ranges from 2.27 to 10.87 kg (Ackenhusen et al., 2001). These mines are buried at shallow depths in the soil, rarely deeper than 10 cm, and are designed to destroy an object in close proximity, such as a person's foot or leg. The targeted object is meant to break into fragments, which can cause secondary damage, such as infection and amputation. Hence, the primary purpose of a blast mine is to injure, rather than kill, the victim in order to increase the logistical (mostly medical) burden on the opposing force.

Blast mines are usually small enough to be carried in one hand. They typically are cylindrical in shape, 5.1-12.7 cm in diameter, and 3.8-7.6 cm in height (Horowitz et al., 1996). Generally, they contain 30-200 g of explosives (Ackenhusen et al., 2001) and their casing may be made of plastic, wood, or sheet metal. Although plastic-encased blast mines are sometimes referred to as "nonmetallic mines", nearly all of them contain some metal parts which are usually the firing pin and a spring/washer mechanism, weighing a gram or so (Horowitz et al., 1996).

3 Modeling

We consider an incident wave u^I , characterized by a propagation speed c , impinging on an inclusion D placed in a homogeneous medium. The inclusion has several physical properties which are different from the ones found in the surrounding medium. The propagation speed in the medium is constant and is denoted by c_0 .

We now introduce the total field u^T , which can be decomposed into the incident and scattered fields, i.e., $u^T = u^I + u^S$. For the moment, we consider the problem to be in d dimensions, with $d = 1, 2, 3$, and assume that the total field satisfies

$$\left\{ \begin{array}{l} \frac{\partial^2 u^T}{\partial t^2} - c^2 \Delta u^T = 0, \quad x \in \mathbf{R}^d, \quad t \geq 0, \\ (u^T - u^I)(t, x) \text{ satisfies a Sommerfeld condition at } \infty, \\ \text{homogeneous initial conditions,} \end{array} \right. \quad (3.20)$$

with the Sommerfeld radiation condition ensuring that the scattered wave is only outgoing at infinity. We recall that this is a condition for the frequency domain problem.

Let Ω denote a bounded domain that surrounds the inclusion D and let Γ_R be the boundary that encloses the domain, as shown in figure 7. We assume that the incident wave u^I is generated by a point source such that after a time T_f , the total field u^T is negligible in Ω . Additionally, we also assume that we have recorded the value of the total field u^T on the boundary Γ_R .

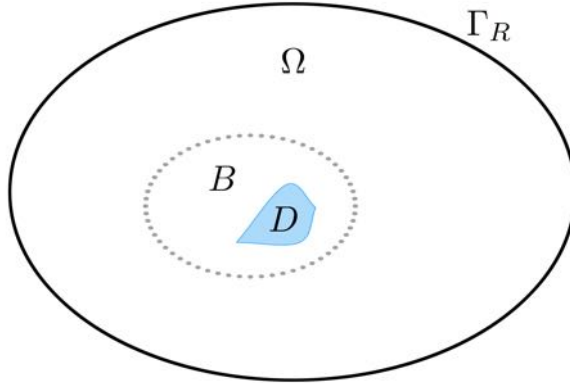


Figure 7: Domain geometry for the generic model.

We consider the field $u_R^T = u^T(T_f - t, x)$ to be the total time reversed field that satisfies the wave equation in (3.20). Our aim is to reconstruct the time reversed field u_R^T from the measurements on Γ_R . For this purpose, we derive a boundary value problem (BVP) whose solution is the time reversed field. It is necessary to point out that neither the exact location nor the physical properties of the inclusion are known. However, we do have knowledge of the physical properties

of the surrounding medium, which, as we had already mentioned in the beginning of this section, has a constant propagation speed c_0 . Thus, the time reversed total field u_R^T satisfies

$$\frac{\partial^2 u_R^T}{\partial t^2} - c_0^2 \Delta u_R^T = 0, \quad (t, x) \in (0, T_f) \times \Omega \setminus D. \quad (3.21)$$

We impose Dirichlet boundary conditions on Γ_R equal to the time reversed recorded fields, i.e., $u_R^T(t, x) = u^T(T_f - t, x)$ on Γ_R . It is also necessary to impose homogeneous initial conditions. However, we lack a boundary condition on the inclusion's boundary in order to define a well-posed BVP for the time reversed field u_R^T in $\Omega \setminus D$. It was mentioned before that the shape and location of the inclusion D are not known. In addition, the type of boundary condition for the hard or soft inclusion is not known either.

In order to overcome these difficulties, the classical approach solves problem (3.21) in the entire domain Ω , assuming that there is no inclusion D , see [15] and references therein. We denote this approximate time reversed solution by w_R^T , which satisfies the equation

$$\frac{\partial^2 w_R^T}{\partial t^2} - c_0^2 \Delta w_R^T = 0, \quad (t, x) \in (0, T_f) \times \Omega,$$

with Dirichlet boundary conditions on Γ_R equal to the time reversed recorded fields. Additionally, we impose the usual homogeneous initial conditions. It is easily verified that the approximate time reversed solution w_R^T differs from u_R^T . Hence, we look for another method.

3.1 Principle of the TRAC Method

We decide to use the approach given in [1, 2, 3] to derive a boundary value problem whose solution is the time reversed scattered field u_R^S . The approach is based on the introduction of a subdomain B enclosing the body D , as shown in figure 7. This subdomain allows us to overcome the unknown inclusion's parameters. However, it is necessary to determine a specific boundary condition for u_R^S on the boundary ∂B so that the solution to this problem will coincide with u_R^S in the restricted domain $\Omega \setminus B$.

In order to derive the boundary condition for u_R^S , we first note that the scattered field u^S is a solution to the problem

$$\left\{ \begin{array}{l} \frac{\partial^2 u^S}{\partial t^2} - c^2 \Delta u^S = 0, \quad x \in \mathbf{R}^d \setminus D, \quad t \geq 0, \\ u^S(t, x) = -u^I(t, x), \quad x \in \partial D, \\ u^S(t, x) \text{ satisfies a Sommerfeld condition at } \infty, \\ \text{homogeneous initial conditions.} \end{array} \right.$$

When the subdomain B is introduced, the scattered field u^S satisfies an exact absorbing boundary condition (ABC) on the boundary of B , i.e., $\text{ABC}(u^S) = 0$ on ∂B . The ABC that we consider is the Bayliss-Turkel first order condition BT^1 , in a three-dimensional space, see [6] and [7]. Applied to the scattered field, this condition reads

$$\text{ABC}(u^S) := \frac{\partial u^S}{\partial t} + c \frac{\partial u^S}{\partial r} + c \frac{u^S}{r} = 0, \quad x \in \partial B, \quad (3.22)$$

being r the radial coordinate with the origin at the center of B . For simplicity, we have assumed that B is a sphere of radius ρ . If we time reverse equation (3.22) using $u_R^S(t, x) = u^S(T_f - t, x)$, we get the expression

$$-\frac{\partial u_R^S}{\partial t} + c \frac{\partial u_R^S}{\partial r} + c \frac{u_R^S}{r} = 0, \quad x \in \partial B. \quad (3.23)$$

We notice that on the boundary of B , $\partial/\partial r = -\partial/\partial n$, where n is the outward normal to the restricted domain $\Omega \setminus B$. The time reversed absorbing boundary condition (TRAC) is obtained by multiplying equation (3.23) by -1 . Thus,

$$\text{TRAC}(u_R^S) := \frac{\partial}{\partial t} (u_R^S(t, \cdot)) + c \frac{\partial}{\partial n} (u_R^S(t, \cdot)) - \frac{c}{r} (u_R^S(t, \cdot)), \quad (3.24)$$

where the minus sign before the last term makes this condition different from the BT^1 absorbing boundary condition. Using this TRAC, we can now derive a boundary value problem whose solution is the time reversed scattered field u_R^S , given by

$$\begin{cases} \frac{\partial^2 u_R^S}{\partial t^2} - c_0^2 \Delta u_R^S = 0, & (t, x) \in (0, T_f) \times \Omega \setminus B \\ \text{TRAC}(u_R^S) = 0, & x \in \partial B, \\ u_R^S(t, x) = u^S(T_f - t, x), & x \in \Gamma_R, \\ \text{homogeneous initial conditions.} \end{cases} \quad (3.25)$$

In [2, 3], a numerical procedure for inclusion identification was deduced from the formulation:

When the subdomain B encloses the inclusion D , then the solution in the restricted domain $\Omega \setminus B$ must be equal to the time reversed solution. Conversely, if the computed solution differs notably from the time reversed solution, it shows that the ball B does not enclose the inclusion D .

As we had already mentioned before, the TRAC is not the standard BT^1 absorbing boundary condition. In addition, it contains an "anti absorbing" term ($-c u_R^S/r$). Therefore, a natural concern arises about the well-posedness of the BVP (3.25). Although a general theory for the TRAC has not been developed, in the next section we present the proof of an energy estimate for a similar problem in a special geometry. It is important to point out that after performing many tests and computations, the authors of the method have never encountered stability problems.

Equation (3.24) shows the definition of the first order TRAC in three dimensions. The time reversed absorbing condition in a two-dimensional space, based on the corresponding BT¹ for this space (see [6, 7]), is given by

$$\frac{\partial u_R^S}{\partial t} + c \frac{\partial u_R^S}{\partial n} - c \frac{u_R^S}{2r} = 0. \quad (3.26)$$

We have assumed so far that the surface B is a sphere or a circle. This assumption simplifies the model and it is usually sufficient to find an approximate location of the object enclosed by the surface. However, in the case of an elongated inclusion, the subdomain B can take the form of an ellipse or spheroidal surface. Absorbing boundary conditions for these cases have been developed in [5], [16], and [17], and, for more general surfaces, in [16, 17]. As shown above, a first order TRAC method simply reverses the sign of the non-differentiated term of the corresponding first order absorbing boundary condition. For a general bounding surface in two dimensions, the first order TRAC is therefore

$$\text{TRAC}(u_R^S) := \frac{\partial}{\partial t}(u_R^S(t, \cdot)) + c \frac{\partial}{\partial n}(u_R^S(t, \cdot)) - \frac{c\kappa}{2}(u_R^S(t, \cdot)), \quad (3.27)$$

where κ is the curvature of the bounding surface B .

3.2 Energy Estimate

Let the trial subdomain B_ρ be a ball of a radius ρ , and denote by r the radial coordinate with the origin at the center of B_ρ . In addition, let g be a real-valued function on ∂B_ρ , and u the solution of the problem

$$\begin{cases} \frac{\partial^2 u}{\partial t^2} - c^2 \Delta u = 0, & \text{in } \Omega \setminus B_\rho, \\ u = 0, & \text{on } \Gamma_R, \\ \frac{\partial u}{\partial t} + c \left(\frac{\partial u}{\partial n} - \frac{u}{\rho} \right) = g, & \text{on } \partial B_\rho, \\ u = u_0, \frac{\partial u}{\partial t} = u_1, & \text{at } t = 0. \end{cases} \quad (3.28)$$

Proposition 3.1 *If Ω is a ball of radius R concentric to B_ρ , we have the following energy estimate written for the BVP (3.28) in spherical coordinates (r, θ, ϕ) :*

$$\begin{aligned} & \frac{1}{2} \frac{d}{dt} \left[\iiint r^2 \sin \phi \left(\frac{\partial u}{\partial t} \right)^2 + c^2 \sin \phi \left(\frac{\partial(ru)}{\partial r} \right)^2 + c^2 \sin \phi \left(\frac{\partial u}{\partial \phi} \right)^2 + \frac{c^2}{\sin \phi} \left(\frac{\partial u}{\partial \theta} \right)^2 \right] \\ & + \iint_{r=\rho} c \rho^2 \sin \phi \left(\frac{\partial u}{\partial t} \right)^2 = \iint_{r=\rho} c \rho^2 \sin \phi \frac{\partial u}{\partial t} g. \end{aligned} \quad (3.29)$$

Proof. The Laplacian in spherical coordinates (r, θ, ϕ) has the form

$$\Delta = \frac{1}{r^2} \frac{\partial}{\partial r} \left(r^2 \frac{\partial(\cdot)}{\partial r} \right) + \frac{1}{r^2 \sin^2 \phi} \frac{\partial^2}{\partial \theta^2} (\cdot) + \frac{1}{r^2 \sin \phi} \frac{\partial}{\partial \phi} \left(\sin \phi \frac{\partial}{\partial \phi} (\cdot) \right). \quad (3.30)$$

The energy estimate is based on an equivalent formulation of the Laplacian (3.30), given by

$$\Delta = \frac{1}{r} \frac{\partial^2}{\partial r^2} (r \cdot) + \frac{1}{r^2 \sin^2 \phi} \frac{\partial^2}{\partial \theta^2} (\cdot) + \frac{1}{r^2 \sin \phi} \frac{\partial}{\partial \phi} \left(\sin \phi \frac{\partial}{\partial \phi} (\cdot) \right). \quad (3.31)$$

We multiply (3.28) by $\partial u / \partial t$ and integrate by parts (recall that $dV = r^2 \sin \phi dr d\theta d\phi$). Only the computation for the term arising from the radial derivative is shown since it is the only non classical one. Hence, we have

$$\begin{aligned} - \iiint \frac{c^2}{r} \frac{\partial^2(ru)}{\partial r^2} \frac{\partial u}{\partial t} r^2 \sin \phi dr d\theta d\phi &= \iiint c^2 \frac{\partial(ru)}{\partial r} \frac{\partial^2(ru)}{\partial r \partial t} \sin \phi dr d\theta d\phi \\ &\quad - \left[\iint c^2 \frac{\partial(ru)}{\partial t} \frac{\partial(ru)}{\partial r} \sin \phi d\theta d\phi \right]_{r=\rho}^{r=R}. \end{aligned}$$

The boundary term at $r = R$ vanishes due to the homogeneous Dirichlet condition on Γ_R . Thus, we decide to focus our attention on the term at $r = \rho$. We have

$$\iint_{r=\rho} c^2 \frac{\partial(ru)}{\partial t} \frac{\partial(ru)}{\partial r} \sin \phi d\theta d\phi = \iint_{r=\rho} c\rho \frac{\partial(ru)}{\partial t} c \left(\frac{\partial u}{\partial r} + \frac{u}{\rho} \right) \sin \phi d\theta d\phi.$$

We know that at $r = \rho$, the equality $\partial/\partial r = -\partial/\partial n$ holds. Using this equality and the second boundary condition in (3.28), we can verify that

$$\begin{aligned} \iint_{r=\rho} c\rho \frac{\partial(ru)}{\partial t} c \left(\frac{\partial u}{\partial r} + \frac{u}{\rho} \right) \sin \phi d\theta d\phi &= \iint_{r=\rho} c\rho \frac{\partial(ru)}{\partial t} \left(\frac{\partial u}{\partial t} - g \right) \sin \phi d\theta d\phi \\ &= \iint_{r=\rho} c\rho^2 \left(\frac{\partial u}{\partial t} \right)^2 \sin \phi d\theta d\phi - \iint_{r=\rho} c\rho^2 \frac{\partial u}{\partial t} g \sin \phi d\theta d\phi. \end{aligned}$$

By rewriting the right-hand side of equation (3.31), we find the energy estimate (3.29). ■

Remark 3.2 *The energy estimate (3.29) is not the standard energy estimate because of the term $(\partial(ru)/\partial r)^2$. We obtain this term by using an equivalent formulation of the Laplacian in spherical coordinates, as mentioned in the proof. This energy estimate proves the well-posedness of the TRAC method but is not physically interpretable.*

3.3 Recreating the Past

The TRAC method's capacity to recreate the past when the line of receivers Γ_R is continuous and encloses the bounded domain Ω , as shown in figure 8(a), was proved in [2] and [3]. For a domain B arbitrarily located in Ω , we solve the problem

$$\begin{cases} \frac{\partial^2 v_R^S}{\partial t^2} - c_0^2 \Delta v_R^S = 0, & (t, x) \in (0, T_f) \times \Omega \setminus B \\ \text{TRAC}(v_R^S) = 0, & x \in \partial B, \\ v_R^S(t, x) = u^S(T_f - t, x), & x \in \Gamma_R, \\ \text{homogeneous initial conditions,} \end{cases} \quad (3.32)$$

with an *ad hoc* artificial boundary condition on the remaining part of the external boundary. When B encloses the object D , we know from the previous section that the solution in the restricted domain $\Omega \setminus B$ coincides with the time reversed solution.

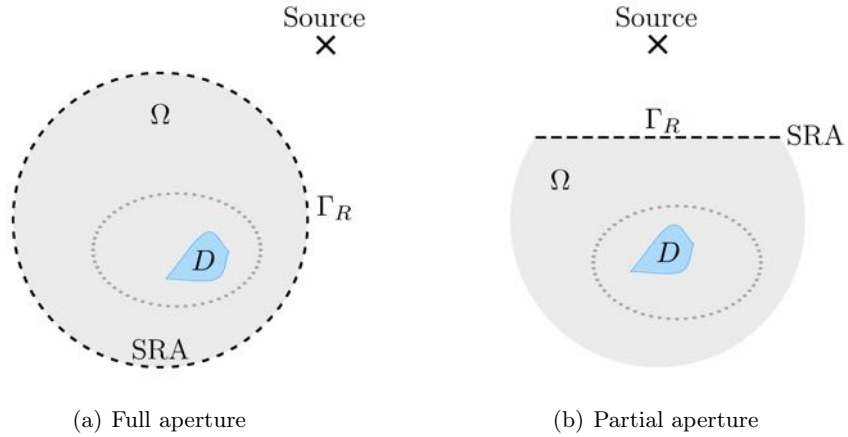


Figure 8: Two configurations of the source-receiver array (SRA). (a) The line of receivers encloses the bounded domain Ω . (b) The aperture is reduced.

The TRAC method also proved to be quite insensitive to the level of noise in the data. A Gaussian noise was added by replacing on Γ_R , the recorded scattered field u^S with

$$u^S = (1 + \text{Coeff} * \text{randn}) * u^S, \quad (3.33)$$

where *randn* satisfies a centered reduced normal law and *Coeff* is the level of noise.

In an attempt to come closer to reality, we now consider a partial aperture, as in figure 8(b), and a finite number of receivers spaced by a fraction of the central wavelength λ . In order to create synthetic data, equation (3.32) is approximated by the FreeFem++ package, which implements a finite element method in space (see [14]).

3.4 Numerical Approximation

In this section, we study the forward and time reversed boundary value problems for the configuration shown in figure 9. Due to the complexity of these problems, it is necessary to use numerical techniques to find their approximate solutions. Thus, for each BVP, we derive a variational formulation and, subsequently, discretize in time and space.

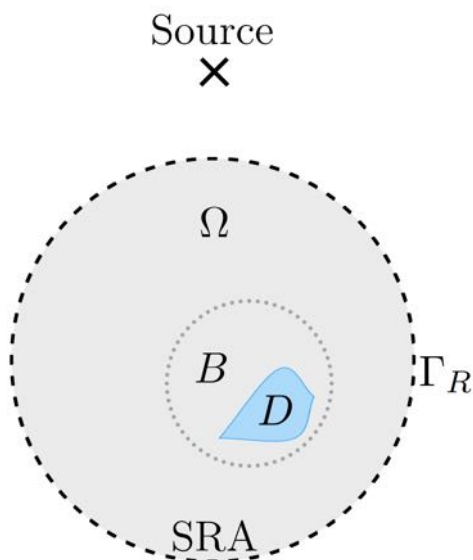


Figure 9: Model geometry.

3.4.1 Forward Problem

Consider the domain $\Omega \subset \mathbf{R}^2$ to be a closed disk of radius R . The total field satisfies

$$\begin{cases} \varepsilon(x) \frac{\partial^2 u^T}{\partial t^2} - \nabla \cdot \left(\frac{1}{\mu(x)} \nabla u^T \right) = 0, & x = (x_1, x_2) \in \Omega, \quad t \in (0, T_f), \\ \frac{\partial u^T}{\partial t} + c(x) \frac{\partial u^T}{\partial n} + c(x) \frac{u^T}{2R} = f(t), & x \in \partial\Omega, \\ \text{homogeneous Cauchy data,} \end{cases} \quad (3.34)$$

where the function $f(t)$ has compact support in time and is defined as

$$f(t) = \begin{cases} [1 - 2\pi^2(\omega t - 1)^2] \exp(-\pi^2(\omega t - 1)^2) & \text{if } t \in (0, T_s) \text{ and } x = x^S \in \mathbf{R}^2, \\ 0 & \text{elsewhere,} \end{cases} \quad (3.35)$$

being ω the frequency of the wave, T_s the duration of the source signal, and $x^S = (x_1^S, x_2^S)$ the source's coordinates.

The functions $\varepsilon(x)$, $\mu(x)$ and $c(x)$ are the dielectric permittivity, magnetic permeability and propagation speed, respectively, as seen in section 2.1. For the moment, we define

$$\varepsilon(x) = \begin{cases} \varepsilon_0 & \text{if } x \in \Omega \setminus D, \\ \varepsilon_D & \text{if } x \in D, \end{cases} \quad \mu(x) = \begin{cases} \mu_0 & \text{if } x \in \Omega \setminus D, \\ \mu_D & \text{if } x \in D, \end{cases} \quad (3.36)$$

and the corresponding propagation speed function as

$$c(x) = \begin{cases} c_0 = \sqrt{\frac{1}{\mu_0 \varepsilon_0}} & \text{if } x \in \Omega \setminus D, \\ c_D = \sqrt{\frac{1}{\mu_D \varepsilon_D}} & \text{if } x \in D. \end{cases}$$

In Section 4, we will extend the previous definitions to the case where there are several layers of homogeneous media and the object D is surrounded by one of these layers.

Variational Formulation

In order for u^T to be in $H^1(\Omega)$, we assume that the function f is at least in $H^{-1}(\Omega)$, i.e., the dual Sobolev space of $H^1(\Omega)$. We will denote the test function space by V , defined as $V = H_0^1(\Omega) = \{v : \Omega \rightarrow \mathbf{R} : v, \nabla v \in L^2(\Omega) \text{ and } v = 0 \text{ on } \partial\Omega\}$. Multiplying the wave equation in (3.34) by a test function $v \in V$ and integrating over Ω , we have

$$\iint_{\Omega} \varepsilon \frac{\partial^2 u^T}{\partial t^2} v - \iint_{\Omega} \nabla \cdot \left(\frac{1}{\mu} \nabla u^T \right) v = 0.$$

Performing an integration by parts on the second integral (divergence theorem), we obtain

$$\iint_{\Omega} \varepsilon \frac{\partial^2 u^T}{\partial t^2} v + \iint_{\Omega} \frac{1}{\mu} \nabla u^T \cdot \nabla v - \int_{\partial\Omega} \frac{1}{\mu} \frac{\partial u^T}{\partial n} v = 0.$$

We use the absorbing boundary condition to replace the normal derivative term and get

$$\iint_{\Omega} \varepsilon \frac{\partial^2 u^T}{\partial t^2} v + \iint_{\Omega} \frac{1}{\mu} \nabla u^T \cdot \nabla v + \int_{\partial\Omega} \frac{1}{c\mu} \frac{\partial u^T}{\partial t} v + \int_{\partial\Omega} \frac{1}{2\mu R} u^T v = \int_{\partial\Omega} \frac{1}{c\mu} f(t) v. \quad (3.37)$$

Hence, we want to find the solution to the following problem:

find $u^T \in V$ such that $\forall v \in V$,

$$\iint_{\Omega} \varepsilon \frac{\partial^2 u^T}{\partial t^2} v + \iint_{\Omega} \frac{1}{\mu} \nabla u^T \cdot \nabla v + \int_{\partial\Omega} \frac{1}{c\mu} \frac{\partial u^T}{\partial t} v + \int_{\partial\Omega} \frac{1}{2\mu R} u^T v = \int_{\partial\Omega} \frac{1}{c\mu} f(t) v. \quad (3.38)$$

Fully Discrete Problem

The variational formulation naturally leads to a semi-discrete problem by approximating the space V by a nonempty finite dimensional space $V_h \subset V$. Since we will use the finite element method, we take V_h to be a space of piecewise linear polynomial functions and problem (3.38) then takes the following form:

$$\begin{aligned} & \text{find } u_h^T \in V_h \text{ such that } \forall v_h \in V_h, \\ & \iint_{\Omega} \varepsilon \frac{\partial^2 u_h^T}{\partial t^2} v_h + \iint_{\Omega} \frac{1}{\mu} \nabla u_h^T \cdot \nabla v_h + \int_{\partial\Omega} \frac{1}{c\mu} \frac{\partial u_h^T}{\partial t} v_h + \int_{\partial\Omega} \frac{1}{2\mu R} u_h^T v_h = \int_{\partial\Omega} \frac{1}{c\mu} f(t) v_h. \end{aligned} \quad (3.39)$$

Let N be the dimension of V_h and $\varphi = (\varphi_l)_{l \in [1, N]}$ a basis of V_h , where φ_l is a P^1 -function vanishing everywhere except on the vertex l . Hence, u_h^T is decomposed on the basis as

$$u_h^T(x) = \sum_l^N U_l \varphi_l(x) \quad \forall x \in \Omega.$$

We now focus on time discretization, where we choose to use centered finite difference schemes. The interest in these schemes is not only the stability they provide but the symmetry they have, which is useful for time reversal techniques. We fix a time step δ and denote

$$(u_h^T)^n(x) \approx u^T(n\delta t, x).$$

Time-discretizing the equation in (3.39) gives

$$\begin{aligned} & \iint_{\Omega} \varepsilon (u_h^T)^{n+1} v_h - 2 \iint_{\Omega} \varepsilon (u_h^T)^n v_h + \iint_{\Omega} \varepsilon (u_h^T)^{n-1} v_h + \delta t^2 \iint_{\Omega} \frac{1}{\mu} (\nabla u_h^T)^n \cdot \nabla v_h \\ & + \frac{\delta t}{2} \int_{\partial\Omega} \frac{1}{c\mu} (u_h^T)^{n+1} v_h - \frac{\delta t}{2} \int_{\partial\Omega} \frac{1}{c\mu} (u_h^T)^{n-1} v_h + \delta t^2 \int_{\partial\Omega} \frac{1}{2\mu R} (u_h^T)^n v_h = \delta t^2 \int_{\partial\Omega} \frac{1}{c\mu} f^n v_h. \end{aligned} \quad (3.40)$$

Matrix Form of the Problem

Consider a discretization mesh \mathcal{T}_h for Ω , conforming around the object D . We define the column vector $U^T = (U_1, U_2, \dots, U_N)^t$. In order to give the matrix form of (3.40), we introduce

- M , which denotes the matrix associated with the bilinear form $: (u, v) \mapsto \iint_{\Omega} \varepsilon uv$, i.e., it is the mass matrix $M_{i,j} = \iint_{\Omega} \varepsilon \varphi_i \varphi_j$
- A , the matrix associated with the bilinear form $: (u, v) \mapsto \iint_{\Omega} \frac{1}{\mu} \nabla u \cdot \nabla v$

Variational Formulation

Let $v \in V$, with $V = H^1(\mathcal{C} \setminus B)$ such that v vanishes on $\partial\mathcal{C}$. We multiply the wave equation in (3.42) by this test function and subsequently integrate over $\mathcal{C} \setminus B$ to obtain

$$\iint_{\mathcal{C} \setminus B} \varepsilon \frac{\partial^2 u^{Tr}}{\partial t^2} v - \iint_{\mathcal{C} \setminus B} \nabla \cdot \left(\frac{1}{\mu} \nabla u^{Tr} \right) v = 0,$$

which, after some manipulation, takes the form

$$\iint_{\mathcal{C} \setminus B} \varepsilon \frac{\partial^2 u^{Tr}}{\partial t^2} v + \iint_{\mathcal{C} \setminus B} \frac{1}{\mu} \nabla u^{Tr} \cdot \nabla v - \int_{\partial B} \frac{1}{\mu} \frac{\partial u^{Tr}}{\partial n} v = 0.$$

We use the first boundary condition in (3.42) to replace the normal derivative term and get

$$\begin{aligned} & \iint_{\mathcal{C} \setminus B} \varepsilon \frac{\partial^2 u^{Tr}}{\partial t^2} v + \iint_{\mathcal{C} \setminus B} \frac{1}{\mu} \nabla u^{Tr} \cdot \nabla v + \int_{\partial B} \frac{1}{c\mu} \frac{\partial u^{Tr}}{\partial t} v - \int_{\partial B} \frac{1}{2\mu\rho} u^{Tr} v \\ &= \int_{\partial B} \frac{1}{c\mu} \frac{\partial u^{Tr}}{\partial t} v - \int_{\partial B} \frac{1}{2\mu\rho} u^{Tr} v + \int_{\partial B} \frac{1}{\mu} \frac{\partial u^{Tr}}{\partial n} v. \end{aligned} \quad (3.43)$$

Fully Discrete Problem

We use a finite element method with P^1 -elements to discretize in space, as in the forward problem presented in Section 3.4.1. The space V is approximated by a nonempty finite dimensional space $V_h \subset V$, consisting of piecewise linear polynomial functions. Let N be the dimension of V_h and $\varphi = (\varphi_l)_{l \in [1, N]}$ a basis of V_h , where φ_l is a P^1 -function vanishing everywhere except on the vertex l . Hence, $u_h^{Tr} \in V_h$ is decomposed on the basis as

$$u_h^{Tr}(x) = \sum_l^N U_l^r \varphi_l(x) \quad \forall x \in \mathcal{C} \setminus B.$$

We now choose to use centered finite difference schemes for time-discretizing. Let δt be the time step and $(u_h^{Tr})^n(x) \approx u^{Tr}(n \delta t, x)$. The time discretization gives

$$\begin{aligned} & \iint_{\mathcal{C} \setminus B} \varepsilon (u_h^{Tr})^{n+1} v_h - 2 \iint_{\mathcal{C} \setminus B} \varepsilon (u_h^{Tr})^n v_h + \iint_{\mathcal{C} \setminus B} \varepsilon (u_h^{Tr})^{n-1} v_h + \delta t^2 \iint_{\mathcal{C} \setminus B} \frac{1}{\mu} (\nabla u^{Tr})^n \cdot \nabla v \\ &+ \frac{\delta t}{2} \int_{\partial B} \frac{1}{c\mu} (u_h^{Tr})^{n+1} v_h - \frac{\delta t}{2} \int_{\partial B} \frac{1}{c\mu} (u_h^{Tr})^{n-1} v_h - \delta t^2 \int_{\partial B} \frac{1}{2\mu\rho} (u_h^{Tr})^n v_h \\ &= \frac{\delta t}{2} \int_{\partial B} \frac{1}{c\mu} (u^{Tr})^{n+1} v_h - \frac{\delta t}{2} \int_{\partial B} \frac{1}{c\mu} (u^{Tr})^{n-1} v_h - \delta t^2 \int_{\partial B} \frac{1}{2\mu\rho} (u^{Tr})^n v_h \\ &+ \delta t^2 \int_{\partial B} \frac{1}{\mu} \left(\frac{\partial u^{Tr}}{\partial n} \right)^n v_h, \end{aligned} \quad (3.44)$$

where u^{Tr} is already known.

Dirichlet Boundary Condition

We now focus our attention on the Dirichlet boundary condition. This is a condition used at every time step and it is therefore preferable to use a penalty approach for it. First, we consider the stationary problem

$$\begin{cases} \nabla \cdot \left(\frac{1}{\mu} \nabla u \right) = 0, & \text{in } \mathcal{C}, \\ u = g, & \text{on } \partial\mathcal{C}. \end{cases} \quad (3.45)$$

The aim of the penalization method is to minimize the functional associated to problem (3.45). Let ϵ be the parameter of penalization. The associated functional has the form

$$\begin{aligned} J : H^1(\mathcal{C}) &\longrightarrow \mathbf{R} \\ v &\longmapsto \frac{1}{2} \iint_{\mathcal{C}} \frac{1}{\mu} |\nabla v|^2 + \frac{1}{2\epsilon} \int_{\partial\mathcal{C}} (v - g)^2. \end{aligned}$$

Thus, u is a solution in $H^1(\mathcal{C})$ of the problem

$$\iint_{\mathcal{C}} \frac{1}{\mu} \nabla u \cdot \nabla v + \frac{1}{\epsilon} \int_{\partial\mathcal{C}} uv = \frac{1}{\epsilon} \int_{\partial\mathcal{C}} gv \quad \forall v \in H^1(\mathcal{C}). \quad (3.46)$$

We need to inject the penalized term into the iterative scheme. This is imposed implicitly and we consider D_{out} to be the matrix associated with the bilinear form : $(u, v) \longmapsto \int_{\partial\mathcal{C}} uv$.

Normal Derivative

A main problem encountered in the discretization is computing the normal derivative. The approach we decided to take is to express with volume integrals the term

$$\delta t^2 \int_{\partial B} \frac{1}{\mu} \left(\frac{\partial u}{\partial n} \right)^n v.$$

We recall that u satisfies

$$\varepsilon(x) \frac{\partial^2 u}{\partial t^2} - \nabla \cdot \left(\frac{1}{\mu(x)} \nabla u \right) = 0, \quad \text{in } (0, T_f) \times \mathcal{C} \setminus B.$$

Thus, for all time independent test functions $w \in H^1(\mathcal{C} \setminus B)$, we get

$$\iint_{\mathcal{C} \setminus B} \varepsilon \frac{\partial^2 u}{\partial t^2} w + \iint_{\mathcal{C} \setminus B} \frac{1}{\mu} \nabla u \cdot \nabla w = \int_{\partial\mathcal{C}} \frac{1}{\mu} \frac{\partial u}{\partial n} w + \int_{\partial B} \frac{1}{\mu} \frac{\partial u}{\partial n} w.$$

Since $v|_{\partial B}$ belongs to $H^{\frac{1}{2}}(\partial B)$ as trace of a function $H^1(\mathcal{C}\setminus B)$, we obtain

$$\int_{\partial B} \frac{1}{\mu} \frac{\partial u}{\partial n} v = \iint_{\mathcal{C}\setminus B} \varepsilon \frac{\partial^2 u}{\partial t^2} w + \iint_{\mathcal{C}\setminus B} \frac{1}{\mu} \nabla u \cdot \nabla w, \quad (3.47)$$

with $w \in H^1(\mathcal{C}\setminus B)$ being a prolongation of $v|_{\partial B}$ that vanishes on the boundary $\partial \mathcal{C}$ and is time independent. Time-discretizing equation (3.47) gives

$$\begin{aligned} \delta t^2 \int_{\partial B} \frac{1}{\mu} \left(\frac{\partial u}{\partial n} \right)^n v &= \iint_{\mathcal{C}\setminus B} \varepsilon (u)^{n+1} w - 2 \iint_{\mathcal{C}\setminus B} \varepsilon (u)^n w \\ &\quad + \iint_{\mathcal{C}\setminus B} \varepsilon (u)^{n-1} w + \delta t^2 \iint_{\mathcal{C}\setminus B} \frac{1}{\mu} (\nabla u)^n \cdot \nabla w. \end{aligned}$$

However, a new difficulty arises in our space discretization with the finite element method since w has constraints on the boundaries.

Matrix Form of the Problem

Consider a conforming discretization mesh \mathcal{T}_h for $\mathcal{C}\setminus B$ and a fixed spacing step h . We define the column vector $U^{Tr} = (U_1^r, U_2^r, \dots, U_N^r)^t$ and set

- M , which denotes the mass matrix $M_{i,j} = \iint_{\mathcal{C}\setminus B} \varepsilon \varphi_i \varphi_j$
- A , the matrix $A_{i,j} = \iint_{\mathcal{C}\setminus B} \frac{1}{\mu} \nabla \varphi_i \cdot \nabla \varphi_j$
- B , the matrix $B_{i,j} = \int_{\partial B} \frac{1}{c\mu} \varphi_i \varphi_j$
- C , the matrix $C_{i,j} = \int_{\partial B} \frac{1}{2\mu\rho} \varphi_i \varphi_j$

Although we keep the same notations as in the forward problem, it is important to keep in mind that the integration domain is different. The matrix form of (3.42) is given by

$$\left\{ \begin{aligned} \left(M + \frac{1}{\epsilon} D_{out} + \frac{\delta t}{2} B \right) (U^{Tr})^{n+1} &= (2M - \delta t^2 A + \delta t^2 C) (U^{Tr})^n + \left(-M + \frac{\delta t}{2} B \right) (U^{Tr})^{n-1} \\ &\quad + \frac{\delta t}{2} B (U^{Tr})^{n+1} - \frac{\delta t}{2} B (U^{Tr})^{n-1} - \delta t^2 C (U^{Tr})^n \\ &\quad + \frac{1}{\epsilon} D_{out} (U^{Tr})^{N_t - (n+1)} + F^n \\ (U^{Tr})^0 &= 0, \\ (U^{Tr})^1 &= 0, \end{aligned} \right. \quad (3.48)$$

where we denote by F^n the discretization of the normal derivative in P^1 . Using matrix notation, each element F_i^n , $i = 1, 2, \dots, N$, of this column vector has the form

$$F_i^n = \begin{cases} \left(M (U^{Tr})^{n+1} - 2M (U^{Tr})^n + M (U^{Tr})^{n-1} + \delta t^2 A (U^{Tr})^n \right)_i & \text{if } i \in \partial B, \\ 0 & \text{if } i \notin \partial B. \end{cases}$$

A similar analysis can be used to obtain the matrix form of the scattered field problem. We use FreeFem++, a language dedicated to the finite element method, to solve system (3.48). In section 4 we present the numerical results that we obtained.

3.5 Criteria

As seen in Section 3.1, if the subdomain B encloses the object D , then the TRAC method is able to recreate the past. On the other hand, when the subdomain does not enclose D , the solution of equation (3.32) does not coincide with the time reversed scattered field $u_R^S = u^S(T_f - t, x)$. This property was used in [1, 2, 3] to locate the inclusion by means of a trial and error procedure. The idea is to modify the location, shape and size of B , with the purpose of approximating the inclusion's location and volume by trial and error. The method relies on mathematical criteria which make it possible to determine if the computed solution of equation (3.32) corresponds to the time reversed scattered field u_R^S or not, and, most importantly, without knowing u_R^S .

In [1, 2, 3], three different criteria were introduced in order to assert that the subdomain B does not enclose D . However, one of them only works for the full aperture case. We will therefore focus on the remaining two since they are effective for a partial aperture.

3.5.1 Absorbing Boundary Condition Criterion

This criterion is derived from the use of absorbing boundary conditions. Indeed, the basis of the method is the time reversed scattered field satisfying $\text{TRAC}(u_R^S) = 0$, at any point outside the inclusion D . In problem (3.32), this relation is used on the boundary of the artificial subdomain B in order to compute v_R^S . If the subdomain B encloses D , both u_R^S and v_R^S coincide. Hence, we have

$$\text{TRAC}(v_R^S) = 0,$$

at any point outside the inclusion (up to approximation errors due to the absorbing condition and the numerical scheme). Thus, we introduce the criterion

$$J_{ABC}(B) := \frac{\left\| \left(\frac{\partial}{\partial t} - c_0 \frac{\partial}{\partial r} \right) v_R^S \right\|_{L^\infty((0, T_f) \times \Omega \setminus B)}}{\left\| \left(\frac{\partial}{\partial t} - c_0 \frac{\partial}{\partial r} \right) u^I \right\|_{L^\infty((0, T_f) \times \Omega)}}, \quad (3.49)$$

being r the radial coordinate with the origin at the center of B . Taking into consideration that this center is somewhat arbitrary, the curvature term in (3.24) was dropped since it could become very large when B is small.

When the trial domain B encloses D , the criterion $J_{ABC}(B)$ should be small. Alternatively, when part or all of inclusion D is outside B , $J_{ABC}(B)$ should be significantly larger than the enclosed case. We notice that this criterion is normalized with respect to the strength of the incident field u^I . Since the computed time reversed scattered field v_R^S depends on the aperture of the SRA, a full aperture will give a stronger signal than a partial aperture. Thus, in order to obtain comparable results, we introduce a relative criterion

$$J_{ABC}^{rel}(B) := \frac{J_{ABC}(\emptyset)}{J_{ABC}(B)}, \quad (3.50)$$

where $J_{ABC}(\emptyset)$ is the criterion computed in the absence of a trial domain B .

3.5.2 Cross-Correlation Criterion

This criterion is inspired from reverse time migration techniques (see [10]). It consists in the cross-correlation of the incident field u^I with the time reversed scattered field v_R^S . In classical applications of earth imaging, the following integral is computed as a function of $x \in \Omega$:

$$f(x) = \int_{t=0}^{t=T_f} v_R^S(T_f - t, x) \times u^I(t, x) dt. \quad (3.51)$$

The function f images the discontinuities of the propagation speed $c(x)$. In this paper, we introduce the related criterion

$$J_{CC}(B) := \frac{\left\| \int_{t=0}^{t=T_f} v_R^S(T_f - t, \cdot) \times u^I(t, \cdot) dt \right\|_{L^\infty(\Omega \setminus B)}}{\left\| \int_{t=0}^{t=T_f} |u^I(t, \cdot)|^2 dt \right\|_{L^\infty(\Omega)}}, \quad (3.52)$$

where v_R^S is the solution to problem (3.32). When the trial domain B encloses D , there is no discontinuity to be imaged in $\Omega \setminus B$ and the criterion $J_{CC}(B)$ should be small. Alternatively, when part of inclusion D is outside B , the function f images this part and $J_{CC}(B)$ is significantly larger than the enclosed case. As for the previous criterion, we define a relative criterion

$$J_{CC}^{rel}(B) := \frac{J_{CC}(\emptyset)}{J_{CC}(B)}, \quad (3.53)$$

where $J_{CC}(\emptyset)$ still refers to the case where there is no trial domain B .

4 Numerical Results

In this section we present several numerical experiments done with the software FreeFem++. All tests have been performed in a two-dimensional computational domain, specifically, in a disk with an absorbing condition on its external boundary simulating an otherwise infinite domain.

4.1 Two Layers

The aim of our first experiments is to investigate the ability of the TRAC method to discriminate a single object from two distinct but close objects buried in dry sand, as shown in figure 10.

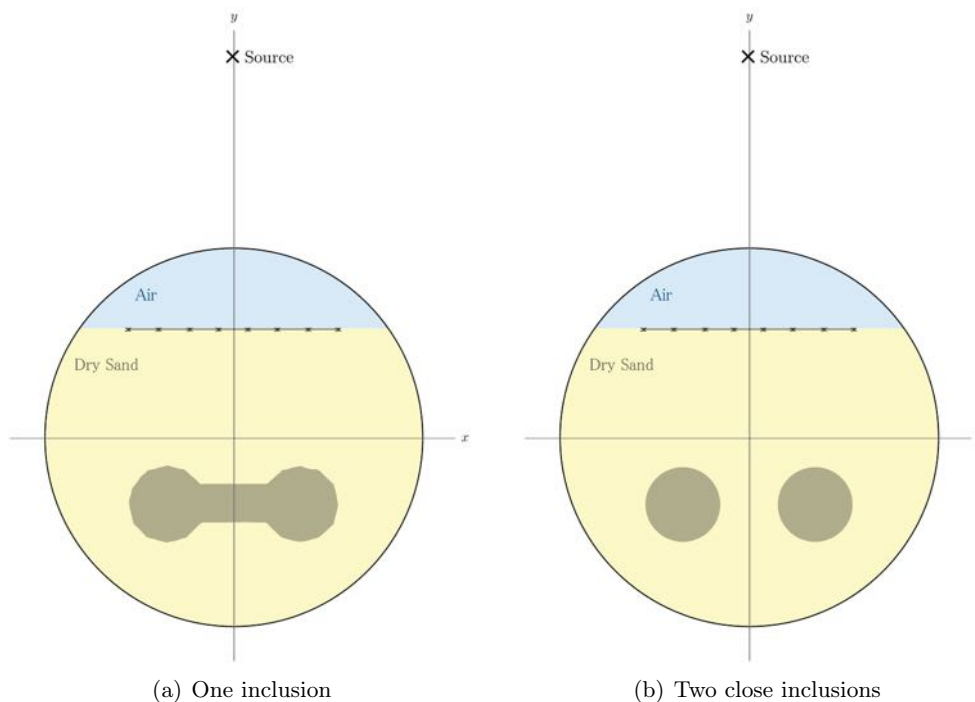


Figure 10: Setup for a two-layered medium.

The propagation medium Ω consists of two homogeneous layers made up of sand and air, i.e., we define $\Omega = \Omega_a \cup \Omega_s$. We consider problem (3.32) with the propagation medium speed (now denoted by c_{2l}) not a constant but piecewise constant

$$c_{2l} = \begin{cases} c_0 = \sqrt{\frac{1}{\mu_0 \varepsilon_0}} & \text{if } x \in \Omega_a, \\ c^s = \sqrt{\frac{1}{\mu^s \varepsilon^s}} & \text{if } x \in \Omega_s. \end{cases}$$

In section 2.1.2, we gave the values for the dielectric permittivity and magnetic permeability of free space or vacuum ($\varepsilon_0 \approx 8.85 \times 10^{-12}$ F/m and $\mu_0 \approx 12.57 \times 10^{-7}$ H/m, respectively).

We recall that these values differ negligibly from the ones in air. Additionally, the relative permittivity term was defined in equation (2.4) and the relative permeability in (2.5). Table 2 presents both absolute and relative values for five materials considered in our tests.

Material	Superscript	ε_r	$\varepsilon = \varepsilon_r \varepsilon_0$	μ_r	$\mu = \mu_r \mu_0$
Air	a	1.0	8.85×10^{-12}	1	12.57×10^{-7}
Iron	f	1.0	8.85×10^{-12}	10,000	12.57×10^{-3}
Plastic	p	1.5	1.33×10^{-11}	1	12.57×10^{-7}
Dry sand	s	3.0	2.66×10^{-11}	1	12.57×10^{-7}
Wet sand	w	5.8	5.13×10^{-11}	1	12.57×10^{-7}

Table 2: Values for the dielectric permittivity and magnetic permeability of five materials.

Material	Superscript	c_r	$c = c_r c_0$	η
Air	a	1	3.00×10^8	376.87
Iron	f	$\sqrt{1/10000}$	3.00×10^6	37,687.40
Plastic	p	$\sqrt{1/1.5}$	2.45×10^8	307.43
Dry sand	s	$\sqrt{1/3.0}$	1.73×10^8	217.38
Wet sand	w	$\sqrt{1/5.8}$	1.24×10^8	156.53

Table 3: Impedances and propagation speeds in five selected materials, with $c_0 \approx 3.00 \times 10^8$.

The propagation speeds for sand, iron and plastic are defined in table 3. An iron object buried in the sand acts like a "hard" inclusion, with a speed ratio given by

$$\frac{c^f}{c^s} = \frac{c_r^f}{c_r^s} = \sqrt{\frac{3}{10000}} \sim 0.017 \ll 1,$$

whereas plastic objects are penetrable with a speed ratio close to 1, since

$$\frac{c^p}{c^s} = \frac{c_r^p}{c_r^s} = \sqrt{2} \sim 1.41.$$

The reflection and transmission coefficients for air and sand can be obtained using equation (2.17) and data in table 3. Thus, we have

$$\Gamma^{a,s} = \frac{\eta^s - \eta^a}{\eta^s + \eta^a} \approx -0.27, \quad \tau^{a,s} = \frac{2\eta^s}{\eta^s + \eta^a} \approx 0.73,$$

where a negative reflection coefficient means that the reflected wave receives a π phase shift.

We consider a source located at 10λ from the center of the computational disk, with λ the source signal wavelength. Since we have two layers, this wavelength is obtained using the relation

$$\lambda = \frac{\min(c^a, c^s)}{\nu},$$

where $\nu = 2\pi/\omega$ is the frequency of the source (3.35) set at 5 GHz. The length of the source-receiver array (SRA) is approximately 5.7λ and the spacing between the receivers is $\lambda/4$, i.e., we have 23 receivers. We study the case of quite far apart inclusions and close inclusions, corresponding to $d = 3\lambda/2$ and $d = \lambda/2$, respectively, being d the distance between the inclusions. For both iron and plastic objects, we aim to distinguish two inclusions ($D = D_1 \cup D_2$) from one inclusion ($D = D_1 \cup D_2 \cup D_3$), as shown in figure 4.1.

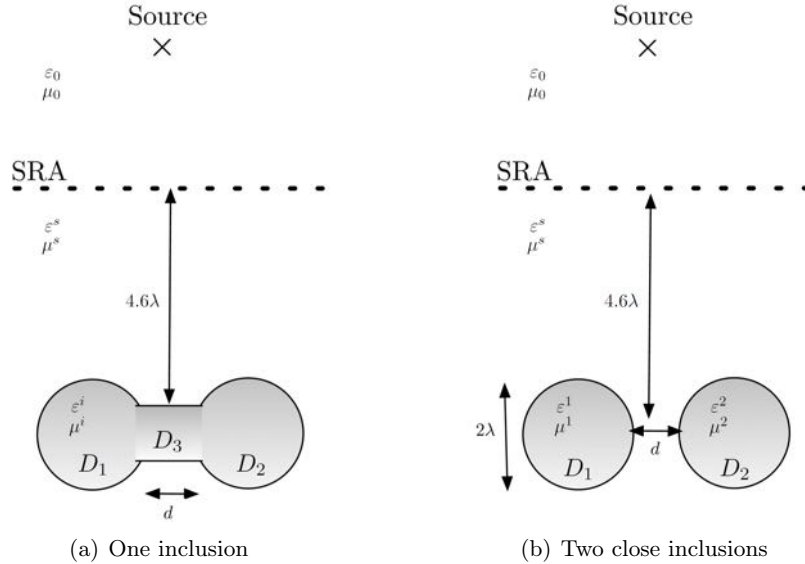


Figure 11: Geometric configuration for a single inclusion and two distinct inclusions.

4.1.1 Iron Objects

We plot in figure 11 the values of the function f defined in (3.51) for $d = 3\lambda/2$. The first row corresponds to two distinct inclusions whereas the second row to a single inclusion. When there is no trial domain, we can see that the cross-correlation function f images clearly the edges of the inclusions, as shown in figure 11(b). However, when the trial domain B encloses the inclusions (top left picture), there is nearly no image, as expected. In addition, when a part of the inclusion is not embedded in B , it is correctly imaged as an illuminated edge (bottom left picture). This illustrates the principle of the TRAC method. Thus, we are able to distinguish between one single inclusion and two close ones.

In figure 12, we show the same configuration of plots for a smaller d equal to $\lambda/2$. When there is no trial domain, the imaging function f is not able to distinguish if there are two inclusions or one, as seen in 11(b). This is due to the proximity of the inclusions. However, in the case of the trial domain enclosing the inclusions (top left picture), the function f is in fact significantly smaller than in the case where B leaves outside part of the inclusion. Note that due to the proximity of the inclusions, we have used trial domains made of two ellipses instead of balls.

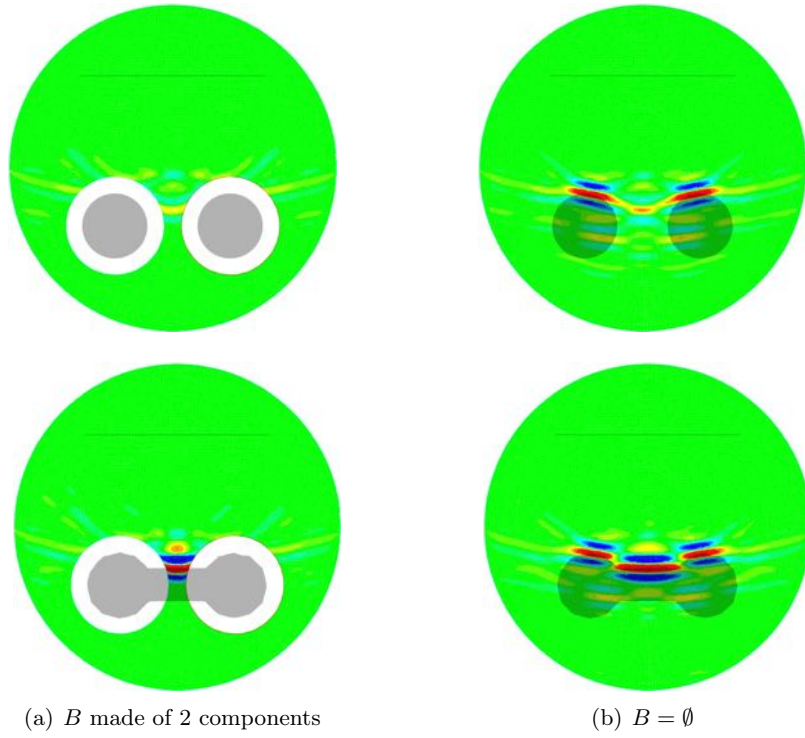


Figure 12: Imaging function (3.51) in a two-layered medium for distant iron objects, $d = 3\lambda/2$.

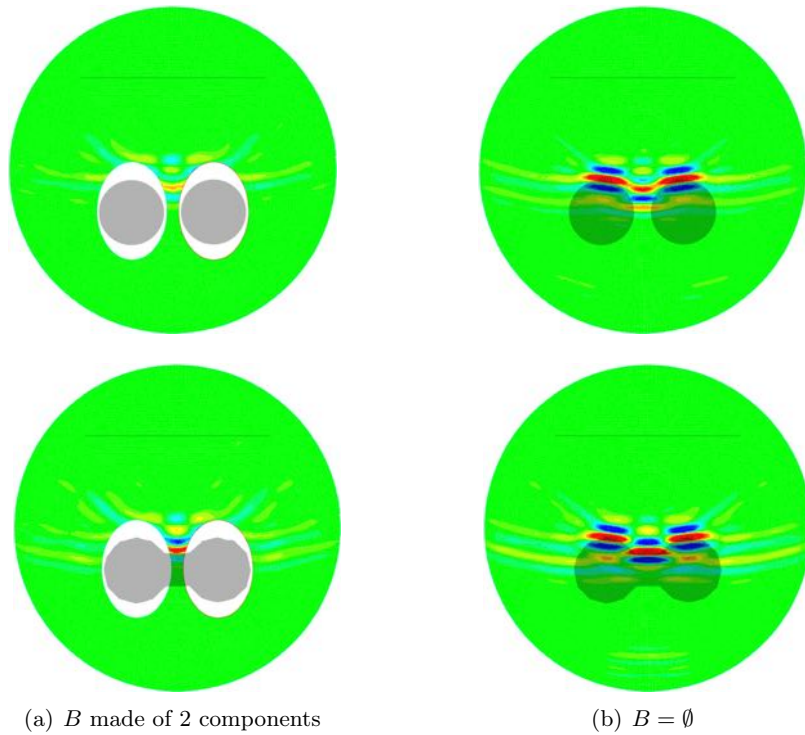


Figure 13: Imaging function (3.51) in a two-layered medium for close iron objects, $d = \lambda/2$.

In order to interpret the previous results from a more quantitative point of view, we give in tables 4 and 5 the values of the criteria J_{ABC}^{rel} and J_{CC}^{rel} for various levels of noise and trial domains B . The first four rows of the tables correspond to the case where the trial domain B is an ellipse that encloses the object D . In the four middle rows, D_2 is outside the trial domain B , and, in the last four rows, the trial domain consists of two ellipses that contain the inclusions D_1 and D_2 , but not D_3 in the case of a single inclusion. We point out that in the latter case, an origin to the trial domain cannot be uniquely defined. Hence, we cannot use the notion of radial derivative at any point in the computational domain and the criterion J_{ABC} is not clearly defined for this case. This is the reason why we put crosses in the tables when the trial domain B is not simply connected.


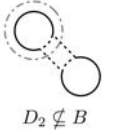
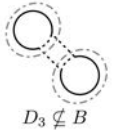
Trial Domain	Noise level	J_{ABC}^{rel}		J_{CC}^{rel}	
		2 Inclusions	1 Inclusion	2 Inclusions	1 Inclusion
 $D \subset B_{\text{ellipse}}$	0%	8.91	14.21	5.26	10.28
	10%	8.05	10.35	5.23	10.19
	20%	5.95	8.54	5.18	10.54
	30%	5.43	7.26	5.49	9.93
 $D_2 \notin B$	0%	1.33	1.70	1.04	0.99
	10%	1.32	1.72	1.04	1.00
	20%	1.32	1.81	1.04	1.01
	30%	1.40	1.74	1.07	1.00
 $D_3 \notin B$	0%	×	×	3.69	1.09
	10%	×	×	3.67	1.09
	20%	×	×	3.84	1.11
	30%	×	×	3.73	1.10

Table 4: Results of two relative criteria in the case of distant iron objects, $d = 3\lambda/2$. Comparison in distinguishing one inclusion from two inclusions for several trial domains.

As seen in Section 3.5, a relative criterion close to one aims to indicate that the trial domain B does not enclose the object D . Alternatively, a significant value for this criterion should indicate that the trial domain B encloses D . For distant iron objects (see table 4), both criteria work as expected, although criterion J_{CC}^{rel} has the advantage to be reliable in all of the cases. Thus, the TRAC method is able to distinguish a simply connected inclusion from an inclusion made of two distant components. In addition, when the distance d becomes smaller, i.e., $d = \lambda/2$, we get similar results (see table 5), and when the trial domain leaves part of the inclusion outside, the values in the bottom right part of table 5 indicate that it is harder but not impossible to distinguish one inclusion from two close inclusions.


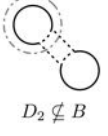
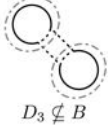
Trial Domain	Noise level	J_{ABC}^{rel}		J_{CC}^{rel}	
		2 Inclusions	1 Inclusion	2 Inclusions	1 Inclusion
 $D \subset B_{\text{ellipse}}$	0%	16.42	16.31	9.29	9.39
	10%	14.53	14.30	9.30	9.27
	20%	7.12	10.54	9.66	9.31
	30%	8.13	7.44	9.69	9.15
 $D_2 \not\subset B$	0%	1.43	2.06	0.91	1.02
	10%	1.43	2.06	0.91	1.02
	20%	1.42	2.05	0.91	1.02
	30%	1.44	2.13	0.91	1.02
 $D_3 \not\subset B$	0%	×	×	3.52	2.14
	10%	×	×	3.56	2.12
	20%	×	×	3.55	2.17
	30%	×	×	3.60	2.10

Table 5: Results of two relative criteria in the case of close iron objects, $d = \lambda/2$. Comparison in distinguishing one inclusion from two inclusions for several trial domains.

4.1.2 Plastic Objects

We now consider plastic objects, which have small reflectivity, i.e., the reflection coefficient for plastic and sand $\Gamma^{p,s} = -0.17$. Figures 14 and 13 are arranged in the same way as figures 11 and 12, respectively. We first focus our attention on distant plastic objects (figure 14). When there is no trial domain B , the cross-correlation function f images the edges of the inclusions. The main difference with the iron objects is that plastic inclusions are penetrable and we can therefore image their back part, although this is barely noticeable in figure 14 due to the relatively small values of the imaging function. Plots in figure 14(a) illustrate the principle of the TRAC method. When the trial domain B encloses the objects (top left picture), there is no significant image. Otherwise, the edges of the part of the inclusion not embedded in B are correctly imaged (bottom left picture). Once again, we are able to distinguish between one single inclusion and two close ones.

Figure 13 shows the case of close plastic objects. Due to the proximity of the inclusions, it is difficult to distinguish two inclusions from one in the absence of a trial domain. When the trial domain B encloses the objects (top left picture), there are no visual imaging values present in the plot. However, when B leaves part of the inclusion (part of D_3) on the outside, we can see a very softly illuminated edge corresponding to the not enclosed part (bottom left picture).

The results from the quantitative analysis are given in tables 6 and 7, organized in the same way as tables 4 and 5, respectively. These tables give the values of the criteria J_{ABC}^{rel} and J_{CC}^{rel} for various levels of noise and trial domains B . For distant plastic objects (see table 6), the values are very similar to the ones obtained for the iron objects. This is an interesting result due to the fact that plastic inclusions are penetrable and iron ones are not. In addition, both

criteria J_{ABC}^{rel} and J_{CC}^{rel} work as expected, the latter having the advantage of being reliable in all situations. The TRAC method is able to distinguish a simply connected penetrable inclusion from one made of two components. When the distance d is smaller ($d = \lambda/2$), it is harder but still possible to distinguish one inclusion from two close ones, as seen in table 7. If we compare the values located in the bottom right part of table 7 with the corresponding ones found in the one-layer case presented in [2] and [3], we notice that the difficulty to distinguish between one single inclusion and two close ones increases with the presence of an additional layer, as expected.


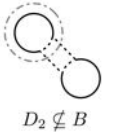

Trial Domain	Noise level	J_{ABC}^{rel}		J_{CC}^{rel}	
		2 Inclusions	1 Inclusion	2 Inclusions	1 Inclusion
 $D \subset B_{\text{ellipse}}$	0%	8.80	12.36	5.24	8.55
	10%	7.57	10.21	5.21	8.41
	20%	5.48	6.41	5.21	8.61
	30%	3.82	4.06	5.07	8.01
 $D_2 \not\subset B$	0%	1.33	1.64	0.99	0.95
	10%	1.33	1.64	0.99	0.94
	20%	1.35	1.74	0.99	0.94
	30%	1.28	1.67	1.00	0.94
 $D_3 \not\subset B$	0%	×	×	3.26	1.01
	10%	×	×	3.28	1.01
	20%	×	×	3.28	1.01
	30%	×	×	3.35	1.01

Table 6: Results of two relative criteria in the case of distant plastic objects, $d = 3\lambda/2$. Comparison in distinguishing one inclusion from two inclusions for several trial domains.




Trial Domain	Noise level	J_{ABC}^{rel}		J_{CC}^{rel}	
		2 Inclusions	1 Inclusion	2 Inclusions	1 Inclusion
 $D \subset B_{\text{ellipse}}$	0%	12.58	11.89	8.43	8.76
	10%	9.88	10.54	8.49	8.51
	20%	9.12	8.69	8.47	8.69
	30%	6.48	5.26	8.27	9.24
 $D_2 \not\subset B$	0%	1.42	1.84	0.90	1.10
	10%	1.40	1.82	0.90	1.10
	20%	1.44	1.85	0.91	1.11
	30%	1.39	1.90	0.90	1.12
 $D_3 \not\subset B$	0%	×	×	3.22	2.17
	10%	×	×	3.28	2.17
	20%	×	×	3.20	2.19
	30%	×	×	3.22	2.19

Table 7: Results of two relative criteria in the case of close plastic objects, $d = \lambda/2$. Comparison in distinguishing one inclusion from two inclusions for several trial domains.

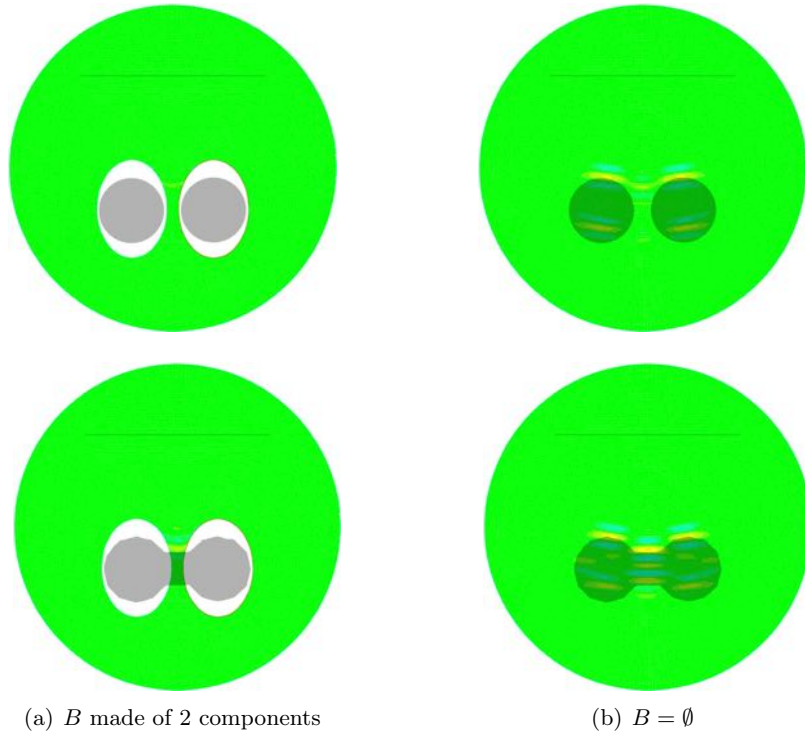


Figure 14: Imaging function (3.51) in a two-layered medium for close plastic objects, $d = \lambda/2$.

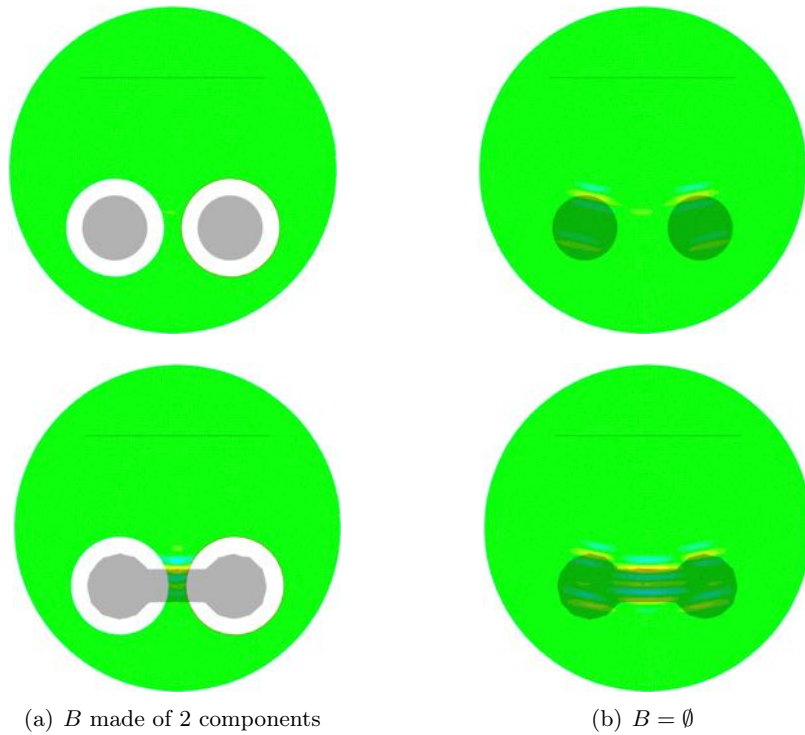


Figure 15: Imaging function (3.51) in a two-layered medium for distant plastic objects, $d = 3\lambda/2$.


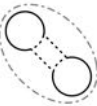


Trial Domain	Noise level	Iron Objects		Plastic Objects	
		2 Inclusions	1 Inclusion	2 Inclusions	1 Inclusion
 $B = \emptyset$	0%	23.04%	41.48%	3.98%	6.64%
	10%	23.07%	41.64%	3.97%	6.62%
	20%	22.99%	42.18%	3.99%	6.61%
	30%	23.46%	41.63%	4.07%	6.56%
 $D \subset B_{\text{ellipse}}$	0%	4.38%	4.04%	0.76%	0.78%
	10%	4.41%	4.09%	0.76%	0.79%
	20%	4.43%	4.00%	0.77%	0.77%
	30%	4.28%	4.19%	0.80%	0.82%
 $D_2 \not\subset B$	0%	22.12%	41.68%	4.02%	7.00%
	10%	22.19%	41.63%	4.02%	7.02%
	20%	22.09%	41.70%	4.02%	7.00%
	30%	21.91%	41.69%	4.07%	6.98%
 $D_3 \not\subset B$	0%	6.24%	38.00%	1.22%	6.54%
	10%	6.29%	38.08%	1.21%	6.55%
	20%	5.98%	38.13%	1.22%	6.55%
	30%	6.29%	37.98%	1.22%	6.52%

Table 8: Non relative criterion J_{CC} (3.52) for distant iron vs. plastic objects in a two-layered medium. Comparison in distinguishing one inclusion from two for several trial domains.

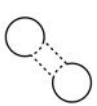



Trial Domain	Noise level	Iron Objects		Plastic Objects	
		2 Inclusions	1 Inclusion	2 Inclusions	1 Inclusion
 $B = \emptyset$	0%	26.81%	30.35%	4.61%	6.25%
	10%	26.87%	30.24%	4.61%	6.22%
	20%	26.91%	30.36%	4.63%	6.31%
	30%	26.86%	29.91%	4.58%	6.26%
 $D \subset B_{\text{ellipse}}$	0%	2.88%	3.23%	0.55%	0.71%
	10%	2.89%	3.26%	0.54%	0.73%
	20%	2.79%	3.26%	0.55%	0.73%
	30%	2.77%	3.27%	0.55%	0.68%
 $D_2 \not\subset B$	0%	29.44%	29.67%	5.09%	5.66%
	10%	29.40%	29.67%	5.11%	5.67%
	20%	29.62%	29.64%	5.09%	5.67%
	30%	29.42%	29.40%	5.11%	5.59%
 $D_3 \not\subset B$	0%	7.61%	14.19%	1.43%	2.88%
	10%	7.55%	14.28%	1.40%	2.87%
	20%	7.59%	13.97%	1.45%	2.88%
	30%	7.46%	14.27%	1.42%	2.85%

Table 9: Non relative criterion J_{CC} (3.52) for close iron vs. plastic objects in a two-layered medium. Comparison in distinguishing one inclusion from two for several trial domains.

In the previous numerical experiments, we have used the same methodology to obtain and present results, for both hard and penetrable inclusions. Moreover, from a quantitative point of view, we observe that the values of the criteria are very similar in both cases of iron and plastic objects. This is due to the normalization based on the criteria obtained in the absence of a trial domain B , see equation (3.53). If one is interested in differentiating iron objects from plastic ones, it is sufficient to consider the non relative criterion J_{CC} , defined by (3.52), since the strength of the field scattered by an iron mine is much larger than the one scattered by a plastic mine. We report in tables 8 and 9 the values of the non relative criterion J_{CC} in the case of iron and plastic objects for $d = 3\lambda/2$ and $d = \lambda/2$, respectively. The first four rows correspond to the classical approach, i.e., when $B = \emptyset$. One observes a factor of five between the iron and plastic objects for the same geometric configuration.

4.2 Three Layers

The objective of the experiments presented in this section is to test the ability of the TRAC method to locate an object buried in dry sand. For more realistic experiments, we now consider the object to be an iron blast mine 10 cm wide and 4 cm tall. As seen in Section 2.2.2, blast mines are usually buried at a depth of 10 cm. As only principal effects are analysed, the mine model is kept simple and the interior design is not accounted for. We consider a two-dimensional domain, consisting of three homogeneous layers made up of air, dry sand and wet sand, i.e., $\Omega = \Omega_a \cup \Omega_s \cup \Omega_w$. The mine is buried in the middle layer, as shown in the detailed geometric configuration presented in figure 15.

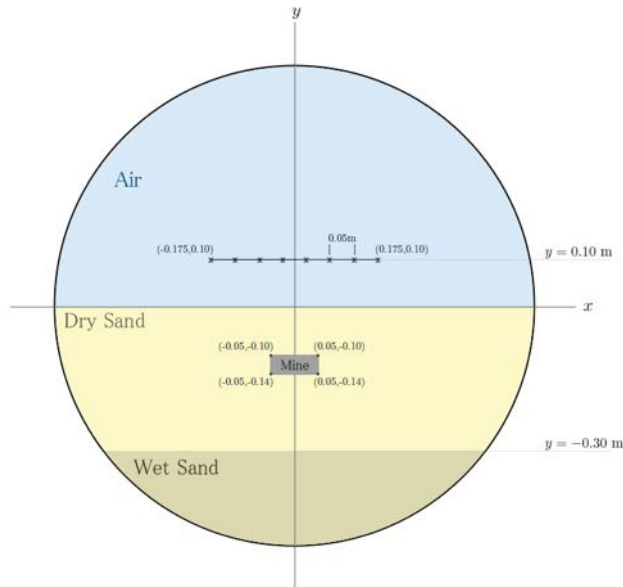


Figure 16: Setup for a three-layered medium.

We consider problem (3.32) with the propagation medium speed (now denoted by c_{3l}) not a constant but piecewise constant

$$c_{3l} = \begin{cases} c_0 = \sqrt{\frac{1}{\mu_0 \varepsilon_0}} & \text{if } x \in \Omega_a, \\ c^s = \sqrt{\frac{1}{\mu^s \varepsilon^s}} & \text{if } x \in \Omega_s. \\ c^w = \sqrt{\frac{1}{\mu^w \varepsilon^w}} & \text{if } x \in \Omega_w. \end{cases}$$

The reflection and transmission coefficients for air and dry sand were given in Section 4.1. Now we need to estimate the coefficients for dry and wet sand, given the additional layer present in the medium. Thus, we have

$$\Gamma^{s,w} = \frac{\eta^w - \eta^s}{\eta^w + \eta^s} \approx -0.16, \quad \tau^{s,w} = \frac{2\eta^w}{\eta^w + \eta^s} \approx 0.84,$$

where the negative reflection coefficient means that the reflected wave receives a π phase shift.

We consider an SRA source located at a height of 10 cm above the air-dry sand interface. The length of the SRA is approximately 35 cm and the spacing between the receivers is 5 cm, i.e., we have 8 receivers. The configuration can be seen in figure 15. The source signal has a central frequency $\nu = 2\pi/\omega$ of 1.5 GHz and the wavelength is given by

$$\lambda = \frac{\min(c^a, c^s, c^w)}{\nu}.$$

In addition, we refine the mesh with respect to the maximal frequency $\nu_{\max} = 3.0$ GHz, allowing us to have a bigger spectrum compared to the one corresponding to the central frequency.

4.2.1 Shifting the Enclosing Ellipse

With our experiments, we aim to determine how the cross-correlation criterion is influenced by the position of an ellipse B , which encloses part or all of the mine D . We take a new coordinate system with origin O' and axis lines x' and y' , and define a shift δ such that the center of the ellipse is in $(x'_c, y'_c) = (-0.05 + 0.10\delta, 0)$, as shown in figure 16. Several tests are then performed by varying the values of δ , i.e., shifting the ellipse along the horizontal axis x' .

In figure 18, we plot the values of the cross-correlation function f , defined in (3.51), for different values of δ . Figure 18(a) refers to the case when more than half of the inclusion is not embedded in B , since $\delta = -1/2$. The plot shows that the edges of the part not embedded in B are correctly imaged. It is evident that as the shift increases, the ellipse encloses more area of the mine and the function f becomes gradually smaller. In the bottom left figure, the mine is centered inside the ellipse and there is no longer a significant image.

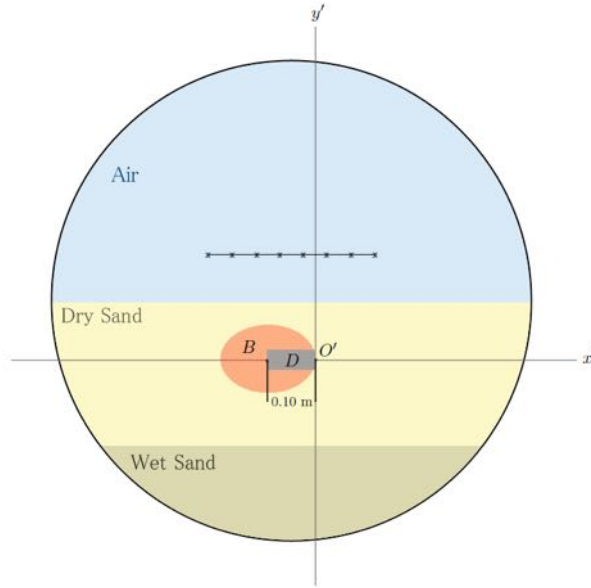


Figure 17: Setup for the mine and ellipse in a new coordinate system.

For a quantitative point of view, we give the absolute and relative values of the cross-correlation criterion in tables 10 and 11, respectively, for the same shifts used to obtain the plots previously discussed. It is clear that as the shift increases, the relative criterion J_{CC}^{rel} also increases, as shown in figure 17. Although only the case with zero noise was graphed, we can infer from table 11 that the rest of the cases behave in a similar way. This means that as the ellipse B encloses more area of the mine, the relative value of the criterion increases, and when the mine is completely enclosed, the relative criterion has a good value. These results are based on the configuration shown in figure 16. Hence, the term "increase" applies for this setup. Independently, we can state that the relative criterion J_{CC}^{rel} is indeed influenced by the position of the trial domain.

Shift δ	$J_{CC}(B)$			
	Noise 0%	Noise 10%	Noise 20%	Noise 30%
- 1/2	11.39	11.37	11.35	11.35
- 1/4	9.81	9.83	9.87	9.77
- 1/8	8.99	8.95	9.02	8.89
- 1/16	8.50	8.49	8.57	8.61
- 1/32	8.23	8.26	8.21	8.16
+ 1/32	7.65	7.66	7.69	7.77
+ 1/16	7.34	7.38	7.38	7.30
+ 1/8	6.71	6.70	6.71	6.63
+ 1/4	6.24	6.25	6.27	6.20
+ 1/2	4.83	4.84	4.80	4.81

Table 10: Non relative criterion J_{CC} (3.52) for an iron mine enclosed by the ellipse B , in a three-layered medium. The ellipse's center is shifted by δ along the horizontal axis.

Shift δ	$J_{CC}^{rel}(B)$			
	Noise 0%	Noise 10%	Noise 20%	Noise 30%
- 1/2	1.17	1.18	1.18	1.18
- 1/4	1.36	1.36	1.35	1.37
- 1/8	1.49	1.49	1.48	1.50
- 1/16	1.57	1.57	1.56	1.55
- 1/32	1.62	1.62	1.63	1.64
+ 1/32	1.75	1.74	1.74	1.72
+ 1/16	1.82	1.81	1.81	1.83
+ 1/8	1.99	2.00	1.99	2.01
+ 1/4	2.14	2.14	2.13	2.16
+ 1/2	2.77	2.76	2.78	2.78

Table 11: Results of the relative criterion J_{CC}^{rel} (3.53) for an iron mine enclosed by an ellipse B , in a three-layered medium. The ellipse's center is shifted by δ along the horizontal axis.

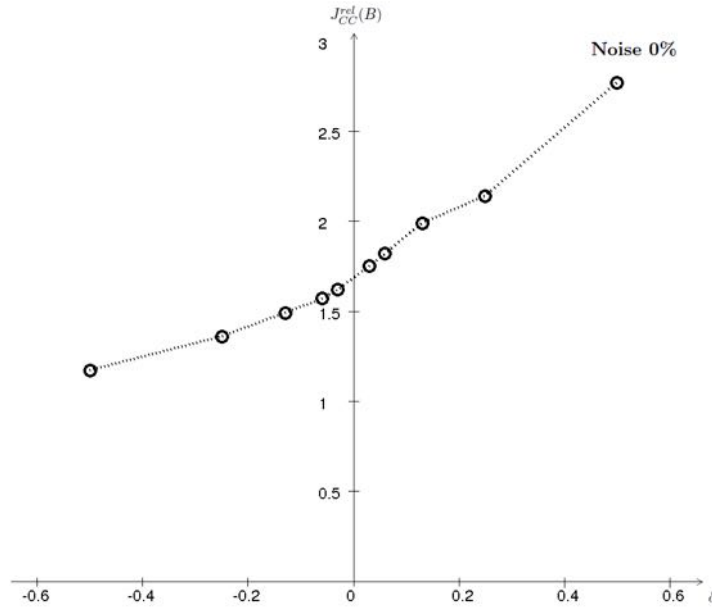


Figure 18: Relative criterion J_{CC}^{rel} (noise 0%) as a function of δ .

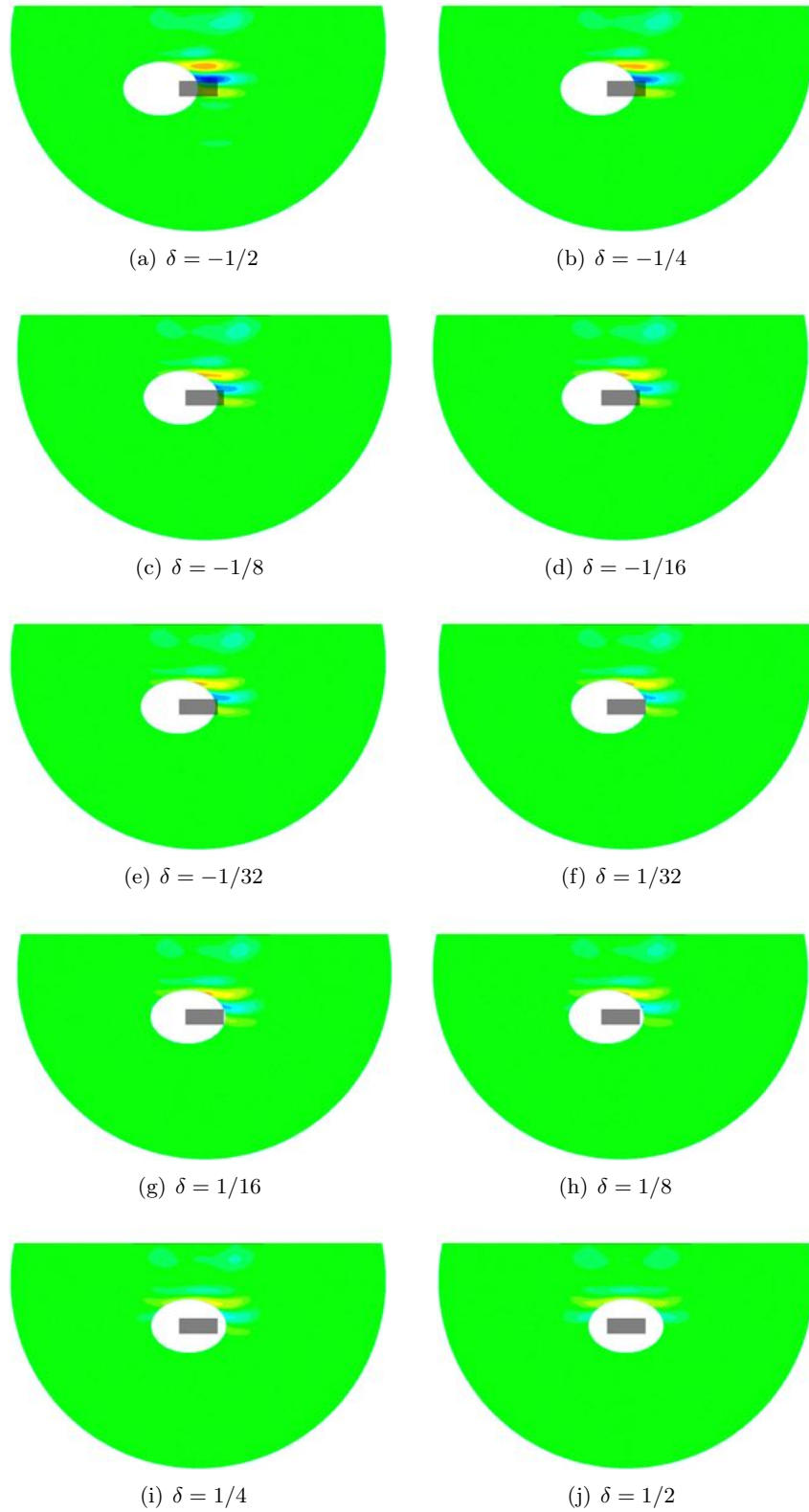


Figure 19: Imaging function (3.51) in a three-layered medium for an iron mine buried in sand and enclosed by an ellipse B . The ellipse's center is shifted by δ along the horizontal axis.

5 Conclusions

This scientific memoir is a continuation and extension of earlier work done in [1], [2], and [3], in which the time reversed absorbing conditions (TRAC) were introduced and used for partial and full apertures. These conditions allow us to recreate the past without knowing the exact location and properties of an inclusion, which diffracts the wave travelling through the medium where it is placed. The TRAC method makes the recreation possible by removing a small region surrounding the scattering inclusion. In this paper, we extend the TRAC method by considering stratified media, specifically, two and three layers made of homogeneous media. Previous work was done using a single homogeneous layer as a medium. However, the goal of this method is to apply it in reality, and it was therefore necessary to perform more realistic tests.

First, we consider the medium to be made up of a layer of air and another of dry sand. The TRAC method is then useful to discriminate a single object from two distinct but close ones buried in the sand. With the addition of the air layer, in comparison to the work done in [1], we notice that the difficulty to distinguish between one single inclusion and two close ones separated by a small distance of $d = 3\lambda/2$ increases, as expected. However, for the rest of the test cases, the results are similar to the ones in [1].

With a configuration consisting of three layers of air, dry sand and wet sand, we get closer to reality. In addition, we consider the object to be a mine and use realistic measures for the setup of the domain. We find that the relative criterion J_{CC}^{rel} is directly influenced by the position of the trial domain enclosing part or all of the mine. As in the case with two layers, the method has proved to be quite insensitive with respect to noise in the data.

We stress that in contrast to many inverse problem methods, the TRAC method does not rely on any *a priori* knowledge of the physical properties of the inclusion. Hard, soft and penetrable inclusions are treated in the same way. We can conclude that the tests in stratified media were successful and worked as expected.

References

- [1] Franck Assous, Marie Kray, and Frédéric Nataf. Time reversed absorbing condition in the partial aperture case.
- [2] Franck Assous, Marie Kray, Frédéric Nataf, and Eli Turkel. Time reversed absorbing condition: application to inverse problems.
- [3] Franck Assous, Marie Kray, Frédéric Nataf, and Eli Turkel. Time reversed absorbing conditions. *Comptes Rendus Mathématiques*, 348(19-20):1063–1067, 2010.
- [4] Claude Bardos and Mathias Fink. Mathematical foundations of the time reversal mirror. *Asymptot. Anal.*, 29(2):157–182, 2002.
- [5] Helene Barucq, Rabia Djellouli, and A. Saint-Guirons. Performance assessment of a new class of local absorbing boundary conditions for elliptical- and prolate spheroidal-shaped boundaries. *Appl. Numer. Anal.*, 59:1467–1498, 2009.
- [6] A. Bayliss and E. Turkel. Radiation boundary conditions for wave-like equations. *Comm. Pure Appl. Math.*, 33(6):707–725, 1980.
- [7] Alvin Bayliss, Max Gunzburger, and Eli Turkel. Boundary conditions for the numerical solution of elliptic equations in exterior regions. *SIAM J. Appl. Math.*, 42(2):430–451, 1982.
- [8] P. Blomgren, G. Papanicolaou, and H. Zhao. Super-resolution in time-reversal acoustics. *J. Acoust. Soc. Am.*, 111:230–248, 2002.
- [9] Nigel J. Cassidy. *Electrical and Magnetic Properties of Rocks, Soils and Fluids. In Ground Penetrating Radar: Theory and Applications*. Jol HM (Ed.), 2009.
- [10] Jon F. Claerbout. *Imaging the Earth's interior*. Blackwell, 1985.
- [11] J. F. Clouet and J. P. Fouque. A time-reversal method for an acoustical pulse propagating in randomly layered media. *Wave Motion*, 25(4):361–368, 1997.
- [12] Arnaud Derode, Philippe Roux, and Mathias Fink. Robust acoustic time reversal with high-order multiple scattering. *Phys. Rev. Lett.*, 75(23):4206–4209, Dec 1995.
- [13] M. Fink. *Renversement du temps, ondes et innovation*. Ed. Fayard, 2009.
- [14] Frédéric Hecht. *FreeFem++*. Numerical Mathematics and Scientific Computation. Laboratoire J.L. Lions, Université Pierre et Marie Curie, <http://www.freefem.org/ff++/>, 3.7 edition, 2010.
- [15] C. Larmat, J.-P. Montagner, M. Fink, Y. Capdeville, A. Tourin, and E. Clévéde. Time-reversal imaging of seismic sources and application to the great sumatra earthquake. *Geophys. Res. Lett.*, 33, 2006.
- [16] Michael Medvinsky and Eli Turkel. On surface radiation conditions for an ellipse. *JCAM*, 234:1647–1655, 2009.
- [17] Michael Medvinsky, Eli Turkel, and Ulrich Hetmaniuk. Local absorbing boundary conditions for elliptical shaped boundaries. *J. Comput. Phys.*, 227(18):8254–8267, 2008.